



HAL
open science

Second sound resonators and tweezers as vorticity or velocity probes : fabrication, model and method

Eric Woillez, Jérôme Valentin, Philippe-E. Roche

► To cite this version:

Eric Woillez, Jérôme Valentin, Philippe-E. Roche. Second sound resonators and tweezers as vorticity or velocity probes : fabrication, model and method. 2023. hal-03927919v1

HAL Id: hal-03927919

<https://hal.science/hal-03927919v1>

Preprint submitted on 10 Jan 2023 (v1), last revised 27 Mar 2023 (v2)

HAL is a multi-disciplinary open access archive for the deposit and dissemination of scientific research documents, whether they are published or not. The documents may come from teaching and research institutions in France or abroad, or from public or private research centers.

L'archive ouverte pluridisciplinaire **HAL**, est destinée au dépôt et à la diffusion de documents scientifiques de niveau recherche, publiés ou non, émanant des établissements d'enseignement et de recherche français ou étrangers, des laboratoires publics ou privés.



Distributed under a Creative Commons Attribution 4.0 International License

Second sound resonators and tweezers as vorticity or velocity probes : fabrication, model and method

Eric Woillez*, Jérôme Valentin[†] and Philippe-E. Roche[‡]

Univ. Grenoble Alpes, CNRS, Institut NEEL, F-38042 Grenoble, France

Distributed under a Creative Commons Attribution.
CC-BY | 4.0 International licence

Abstract

An analytical model of second-sound resonators with open-cavity is presented and validated against simulations and experiments in superfluid helium using a new design of resonators reaching unprecedented resolution. The model accounts for diffraction, geometrical misalignments and flow through the cavity. It is validated against simulations and experiments using cavities of aspect ratio of the order of unity operated up to their 20th resonance in superfluid helium. An important result is that resonators can be optimized to selectively sense the quantum vortex density carried by the throughflow -as customarily done in the literature- or alternatively to sense the mean velocity of this throughflow. Two velocity probing methods are proposed, one taking advantage of geometrical misalignments between the tweezers plates, and another one by driving the resonator non-linearly, beyond a threshold entailing the self-sustainment of a vortex tangle within the cavity.

After reviewing several methods, a new mathematical treatment of the resonant signal is proposed, to properly separate the quantum vorticity from the parasitic signals arising for instance from temperature and pressure drift. This so-called *elliptic method* consists in a geometrical projection of the resonance in the inverse complex plane. Its strength is illustrated over a broad range of operating conditions.

The resonator model and the elliptic method are applied to characterize a new design of second-sound resonator of high resolution thanks to miniaturization and design optimization. When immersed in a superfluid flow, these so-called *second-sound tweezers* provide time-space resolved information like classical local probes in turbulence, here down to sub-millimeter and sub-millisecond scales. The principle, design and micro-fabrication of second sound tweezers are detailed, as well as their potential for the exploration of quantum turbulence

Contents

1	Introduction to second sound resonators	2
1.1	Quantum fluids and second sound	2
1.2	Generation and detection of second sound waves	2
1.3	From macroscopic second sound sensors to microscopic tweezers	3
1.4	Overview of the manuscript	4
2	Design, fabrication and mode of operation of second sound tweezers	4
2.1	Mechanical design	4
2.2	Second sound detection and generation	7
2.2.1	Thermometry	7
2.2.2	Heating	8
2.2.3	Digression on the operation in the non-linear heating regime	9
2.3	Microfabrication and assembling	10
2.4	Electric circuit	13

*present affiliation: CEA-Liten, Grenoble

[†]present affiliation: Observatoire de Paris - PSL, CNRS, LERMA, F-75014, Paris, France

[‡]Corresponding author

3	Models of second sound resonators	14
3.1	Resonant spectrum of second sound resonator: phenomenological aspects	15
3.2	Analytical approximations	15
3.3	Numeric algorithm	19
3.3.1	For a background medium at rest	19
3.3.2	In the presence of a turbulent flow	21
3.4	Quantitative predictions	22
3.4.1	Spectral response of second sound resonators	23
3.4.2	Response with a flow	23
3.4.3	Effect of lateral shift of the emitter and receiver plates	26
3.4.4	Limits of the model	27
3.5	Quantum vortex or velocity measurements ?	28
4	Measurements with second sound tweezers	29
4.1	The vortex line density from the attenuation coefficient	30
4.2	Analytical method in an idealized case	32
4.3	The elliptic method	33
4.4	Applications of the elliptic method	35
4.4.1	Suppression of temperature and pressure drifts	35
4.4.2	Measure of vortex line density fluctuations	36
4.4.3	Filtering the vibration of the plates	38
4.5	Velocity measurements	38
5	Summary and Perspectives	40

1 Introduction to second sound resonators

1.1 Quantum fluids and second sound

Below the so-called lambda transition, liquid ${}^4\text{He}$ enters a quantum state named He-II. This liquid transition occurs around $T_\lambda \simeq 2.18\text{ K}$ at saturated vapor conditions. According to Tisza and Landau *two-fluid model*, the hydrodynamics of He-II can be described as the hydrodynamics of two interpenetrating fluids, called the superfluid component and the normal fluid component [Bal07, Gri09]. The superfluid density ρ_s is vanishingly small right below the transition, and it increases as temperature decreases. The opposite dependence occurs for the normal fluid density ρ_n , which becomes vanishingly small in the zero temperature limit. The properties of both fluids strikingly differ. The superfluid has zero viscosity and zero entropy. Besides, the circulation of its velocity field is quantized in units of $\kappa = h/m \simeq 0.997 \cdot 10^{-7} \text{ m}^2/\text{s}$, where h is Planck constant and m the atomic mass of ${}^4\text{He}$. This quantization constrain results in the existence of filamentary vortices of Ångströmic diameter, later referred to as the superfluid or quantum vortices[Don91]. Contrariwise, the normal fluid follows a classical viscous dynamics and carries all the entropy of the He-II[Put74, Kha00].

The existence of distinct velocity fields \mathbf{v}_s and \mathbf{v}_n for the superfluid and normal fluid results in the existence of two independent sound modes in He-II, as can be shown by linearizing the equations of motion [Put74, Kha00, Don09]. The so-called “first sound” corresponds to a standard acoustic wave : both fluids are oscillating in phase ($\mathbf{v}_s = \mathbf{v}_n$), producing oscillations of the local pressure and density $\rho = \rho_s + \rho_n$. The “second sound” corresponds to both fluids oscillating in antiphase without net mass flow ($\rho_s \mathbf{v}_s = -\rho_n \mathbf{v}_n$). Hence, the relative densities of superfluid and normal fluid locally oscillates, as well as entropy and temperature.

1.2 Generation and detection of second sound waves

Experimentally, two techniques are mostly used to generate and detect second sound: one mechanical and the other thermal. Alternative techniques not discussed here have been occasionally used, including optical scattering (e.g. [PGB70]) and acoustic detection above the liquid-vapor interface[LFF47] or in the flow itself (e.g. [HR76]).

The mechanical technique consists in exciting and sensing a single component of He-II, either its superfluid one or the normal fluid component. Indeed, a single fluid motion can be viewed as a superposition of a second sound and a first sound (i.e. an acoustic wave), with an exact compensation of motion for one of the two fluids at the location of the transducer. Since the first sound velocity is typically one decade larger than the second second velocity[DB98], most second sound resonances don’t coincide with acoustic resonances. In practice, a selective displacement of the superfluid component is achieved in *Peshkov transducers*. They are made of a standard acoustic transducer side-by-side with a fixed porous membrane-filter which tiny pores are viscous dampers for the normal fluid but are transparent (“*superleaks*”) for the superfluid [Pes48, HL88]. Alternatively,

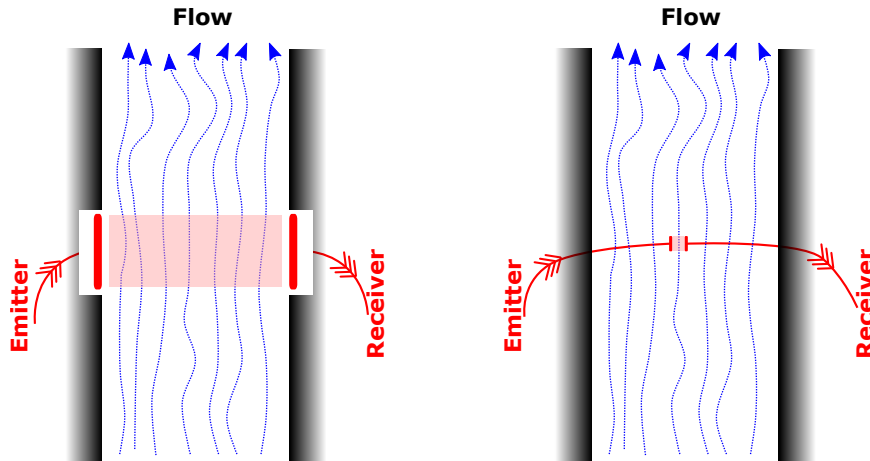


Figure 1: **Left:** A macroscopic resonator for second sound, embedded in the sidewall, is used to sense the averaged flow properties in the shaded region. **Right:** Second sound tweezers. In contrast with the macroscopic design of the left schematics, this miniaturized resonator, positioned within the flow, allows space and time resolution of the flow variations.

a selective displacement of the normal fluid component is achieved in *oscillating superleak transducers*. They are based on a vibrating porous membrane that is coupled to the motion of normal fluid by viscous forces, and uncoupled to the inviscid superfluid. They can be manufactured by replacing the membrane of a loudspeaker or microphone by a millipore or a nucleopore sheet [WBF⁺69, SE70, DLL80].

The thermal technique to generate and detect second sound consists in forcing second sound by Joule effect, and detecting it with a thermometer. Depending on the operating range of temperature and practical considerations, several types of thermometers can be suitable to detect second sound waves. The literature being vast, we only list a few thermistor materials and bibliographic entry points. Materials with a negative temperature coefficients¹ include carbon in various forms (*aquadag* paint, fiber, pencil graphite,..) [HVS01], doped Ge[Sny62], RuOx [YI18], ZrN_x/Cernox [YYK97, FS04] and Ge-on-GaAs [MMP⁺07]. Transition edge superconductor thermometers are often preferred when large sensitivity or low resistivity is important, for instance Au₂Bi [Not64], PbSn [CR83, RR01], granular Al [CA68, MSS76] and AuSn [Not64, Lag76, BSS83]. More information on AuSn is provided in section 2.2.1. The second sound tweezers presented in the present study resorts to this thermal technique, both for generation and detection of second sound².

1.3 From macroscopic second sound sensors to microscopic tweezers

In the presence of superfluid vortices, the superfluid and normal fluid experience a viscous mutual coupling [Don91], which entails a damping of the second sound waves. This attenuation of second sound by vortices have been extensively used as a tool to explore the properties of He-II flows over the last 60 years[Vin57], in particular to explore the properties of quantum turbulence (e.g. see [VJSS19]), a field of applications which as motivated the development of second sound tweezers. For example, mechanical second sound transducers were successfully used to study the turbulence of He-II in the wake of a grid by groups in Eugene, Prague and Tallahassee (e.g. see [SNVD02, BVS⁺14, MG18]). Examples of thermal second sound transducers successfully used to study turbulence of He-II flows are described in studies by groups from Paris, Tallahassee, Grenoble and Gainesville (e.g. see [WPHE81, HVS92, RDD⁺07, YI18]).

A specific type of probe allows very sensitive probing of the density of quantum vortices in He-II flow : standing-wave second sound resonators. Such a resonator consists in two parallel plates facing each other, one functionalized with a second sound emitter and the other with a receiver. The emitter excites the cavity at resonance to benefit from the amplification of the cavity. The characteristics of the standing wave between the plates provides information on the properties of the fluid and flow between the plates, in particular the density of vortex lines, which impacts the amplitude of the standing wave. Aside from vortex density measurements, the second sound can also provide information on the fluid temperature -since the second sound velocity depends on it- and on the velocity of the background He-II flow when it induces a phase shift or Doppler effect on the second sound (e.g. see [DL77, WPHE81, WVR21]).

The characteristics listed above for the standard (macroscopic) second sound resonators remain relevant for their miniaturized version : second sound tweezers. Beside miniaturization, a key specificity of tweezers is their

¹Phosphor bronze wire, a positive temperature coefficient thermometer has also been used in the early days [Pes46].

²In principle, mechanical and thermal techniques could be combined to generate and detect, although we are not aware of any composite configuration reported in the literature.

low footprint on the streamlines when positioned in the core of a flow. This key differences between standard and tweezers resonators are sketched in figure 1. Consequently, standard resonators provide information on averaged properties of the flow, while tweezers give access to space and time resolved information. Thus, tweezers are local probes in the same ways as the hot-wire anemometers or cold-wire thermometers used in turbulence studies.

In the present design for tweezers, the thermal actuation technique is preferred to the mechanical actuation because it makes it easier to respect the constrains of miniaturization and reduced flow blockage.

1.4 Overview of the manuscript

The following sections cover independent topics,

Section 3 presents a comprehensive modelling of second-sound resonators accounting for plate misalignment, advection, finite size and near field diffraction. Diffraction, which has been neglected in previous quantitative models, turns out to be a dominant source of degradation of the quality factor in our case studies. Applications to the measurement of vortex concentration or velocity are considered.

Section 4 presents existing methods to process the signal from second sound resonators, and their limits. To circumvent them, we introduce a new general approach, named the *elliptic method*, based on a mathematical properties of resonance. This method allows to dynamically separate the amplitude variations of the standing wave due to variations of vortex density or variations of velocity, from the phase variations (more precisely, from the acoustical path variations), for instance due to variations of the second sound velocity themselves resulting from a temperature drift.

Section 2 reports the design, clean-room fabrication and operation of miniaturized second-sound resonators, named *second-sound tweezers*. These tweezers allow to probe the throughflow of helium with an unprecedented spatial and time resolution.

For better clarity, we first present the second-sound tweezers, which allows to illustrate the topics on modelling and method with a challenging practical case. Though we emphasize that the modelling and methods introduced in this article are general and relevant to second-sound resonator regardless of their size, including the macroscopic sensors embedded in parallel walls encountered in the literature.

2 Design, fabrication and mode of operation of second sound tweezers

The core part of second sound tweezers is a stack composed of a heating cantilever and a thermometer cantilever, separated by a spacer (see Figs. 2 and 3). Heaters and thermometers are cantilevers composed of a baseplate, an elongated arm and a tip. The baseplate is the thickest part while the tip is the thinnest one. The active areas, the emitter and receiver plates, are located on the tips. For a given device, heater and thermometer have strictly the same mechanical structure, the only difference between them being the chemical elements used in the serpentine electrical path deposited on the tip. Three cantilever types were fabricated in order to allow assembling of resonators with three different tip sizes (see Fig.4). The tip widths are 1000 μm , 500 μm and 250 μm .

Next subsection 2.1 presents considerations which prevailed in the mechanical design of the second sound tweezers. The following one (section 2.2) discusses the detection (thermometry) and generation (heating) of second sound by the tweezers. The last two subsections present the microfabrication techniques (section 2.3) and the electrical circuitry used to operate the probes (section 2.4).

2.1 Mechanical design

Resolution. The tweezers space-resolution L_{res} is set by the largest dimension of its cavity, which can be either the inter-plates distance D , also called the “gap”, or the side length L of the plates here assumed to be squared shaped. The present study mostly focuses on cavities with an aspect ratio of order 1, to benefit from optimal space averaging of the signal at given space-resolution. The tweezers time-resolution τ_{res} is set by the decay-time of a wave bouncing between the plates. In section 3.2, we introduce and validate a simple model accounting for dissipation in the cavity due to diffraction loss and residual inclination of the plates. An upper bound for τ_{res} is obtained from the diffraction loss term: $\tau_{\text{res}} \simeq L^2 f / bc_2^2$, where $b \approx 0.38$, c_2 is the second sound velocity and f is the wave frequency which can be approximated as $nc_2/2D$ for the n^{th} mode of resonance (see eq.6). Thus, the tweezers time-resolution due to diffraction loss can be estimated as

$$\tau_{\text{res.}} \simeq \frac{L^2 f}{bc_2^2} \simeq n \frac{L^2}{Dc_2}$$

The ratio $L_{\text{res}}/\tau_{\text{res}}$ of the space resolution and time resolution defines a characteristic velocity for which the probe optimally averages the space-time fluctuations. For instance, in cavities of aspect ratio one ($D = L$) operated on its n^{th} resonance, the nominal velocity is estimated as c_2/n . These estimates show that cavities

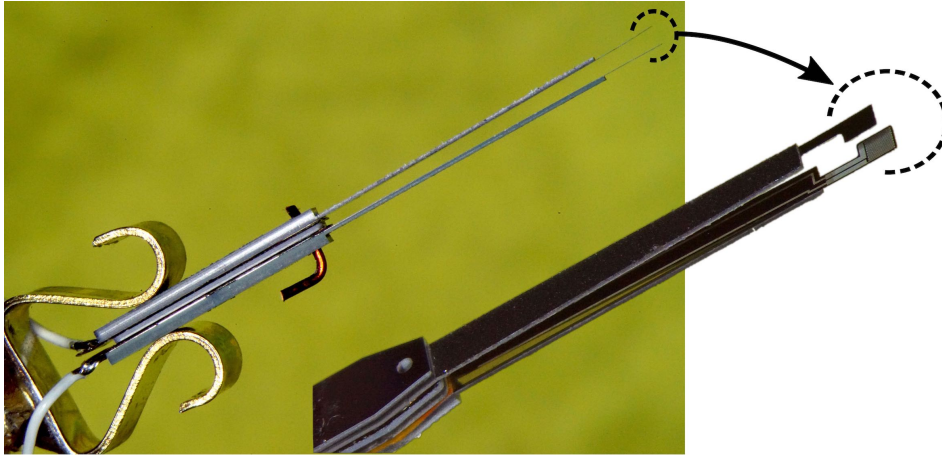


Figure 2: Second sound tweezers, pictured from two angular perspectives. (Left) Probe as seen in the direction of the mean flow (or nearly so). The second sound cavity is localized at the upper tip of the probe, in the encircled area. The bend copper wire through the probe is a temporary *joystick* used for a fine-alignment of cavity plates under the microscope. The two coaxial cables for heating and thermometry are visible in the lower left corner of the picture. (Right) The picture insert shows the same probe after some rotation, and after removal of the *joystick*, making visible the through-hole across the silicon stack. The two staggered notches used for thermal confinement of the standing wave in the cavity are clearly apparent.

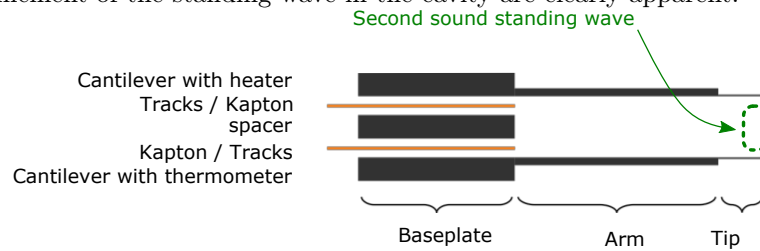


Figure 3: Schematic side view of the constitutive stack of second sound tweezers (the pieces are shown separated for illustration, their thicknesses are exaggerated). The active areas, the emitter and receiver plates, are constituents of the tip.

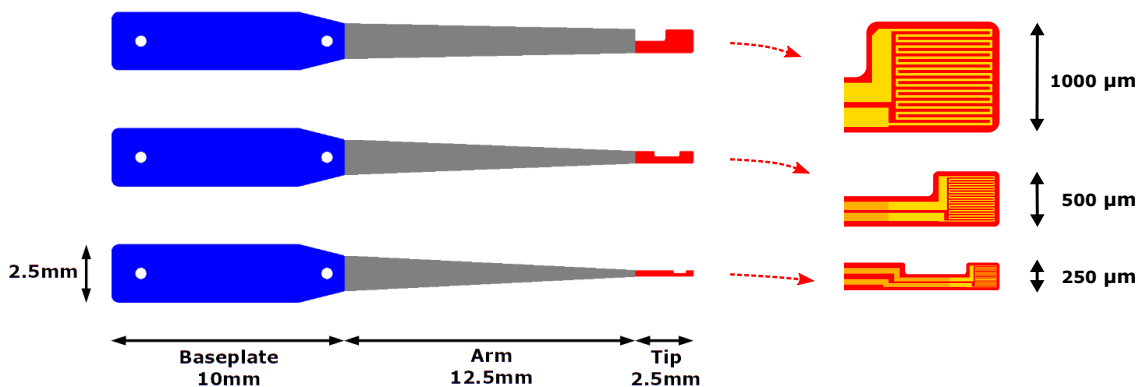


Figure 4: Top view of the 3 cantilever types. The tips widths are respectively 1000 μm , 500 μm and 250 μm . **Left:** Mechanical structures, all parts are silicon made, different thicknesses are represented by different colors. The baseplate width is 2.5mm for all types. **Right:** Electrical path on each tip type. Yellow areas are a deposition of TiPt for heaters and AuSn for thermometers. Orange areas are a thick AuPt deposition for current leads.

with aspect ratio of order unity are fittingly sized for second-sound-subsonic flow, that is flows with a mean velocity of few m/s .

Blocking effect. The above considerations on space resolution are relevant if the measured flow is not altered by the probe support. The present design conforms to the empirical $\times 10$ rule stating that components of the support that obstruct the flow on a length scale \mathcal{X} should be positioned at least $10\mathcal{X}$ away from the measurement zone. Accordingly, the cavity is at the end of elongated arms and the cantilevers are 25 mm in length of decreasing thicknesses and widths, as illustrated by the picture of Fig.2 and by Figure 3. The thickness successive values are around $520\mu m$, $170\mu m$ and $20\mu m$ while the width decreases from 2.5mm to $145\mu m$ in the narrowest zone (resp. $275\mu m$ and $500\mu m$) for cavities with $L = 250\mu m$ (resp. $L = 500\mu m$ and $L = 1000\mu m$).

Wave confinement. The spatial resolution of tweezers would be degraded if the second sound standing wave was spreading out of the $L \times L \times D$ cavity, by reflection between the supporting arms. A design trick was implemented to confine the standing wave in the cavity region by breaking the mirror symmetry between the two cantilevers. Thus, as shown in Fig.2, anti-symmetric notches in the tips prevent the second sound to escape by bouncing away from the cavity, at least in the geometric-optic approximation where diffraction is neglected.

Mechanical resonances. Besides the $\times 10$ rule consideration, these dimensions are chosen such that the mechanical vibrations of the arm are pushed up to $\sim 1 kHz$ or above. The fundamental resonance frequency of the trapezoidal-shaped arm in vacuum was estimated from the analytical formula in [Lob07] (section 1.3.1.1).

$$f_0 = \frac{8.367}{2\pi} \frac{e}{t^2} \sqrt{\frac{E_{Si}(3w_2 + w_1)}{\rho_{Si}(49w_2 + 215w_1)}}$$

We find $f_0 = 2195 Hz$ (resp. 1889 Hz and 1569 Hz) using the material properties $E_{Si} = 140 GPa$, $\rho_{Si} = 2330 kg/m^3$ and the dimensions of the intermediate section of the arm having thickness $e = 172\mu m$, length $t = 12.5 mm$, and width decreasing from $w_2 = 1.5 mm$ to $w_1 = 250\mu m$ (resp. to $500\mu m$ and $1000\mu m$). An experimental validation was done at room temperature in air with an arm with $w_1 = 1000\mu m$. Its mechanical vibration frequency spectrum was measured from a photoreceptor detecting a laser beam reflecting of the arm. The mechanical excitation was provided either by hitting the table supporting the set-up with a small hammer or by pointing a jet of compressed air toward the arm. In both cases, the fundamental mechanical resonance frequency was found to be 1215 Hz, in reasonable agreement with the 1569 Hz prediction given the uncertainty on the Young modulus and deviations from the trapezoidal shape. As discussed in 4.4.3, indirect measurements of the resonance frequency were done in $1.2 m/s$ superfluid flow and gave $f \approx 825 Hz$, $f \approx 1050 Hz$ and an amplitude of vibration smaller than $1\mu m$. The decrease in frequency compared to room-temperature measurement is interpreted as mostly due to a fluidic added mass effect[Sad98].

Deflection of the tips' ends. The thicknesses of the tweezers parts are such that the mechanical deflection at the tip endpoint remains significantly lower than the inter-plate distance under typical operating conditions.

The deflection at the tip endpoint can be estimated by considering separately the arm deflection (with thickness $172\mu m$) and the tip deflection (with thickness $20\mu m$). As a first approximation, both arm and tip are considered as cantilever beams of uniform width submitted to a uniformly distributed load, and having one embedded end and one free end. This geometrical approximation overestimates the deflection of the arm, as its endpoint is narrower than its base, and it underestimates the deflection of the tip, as the notch is ignored. Still, this is enough to get order-of-magnitude estimates. The load is estimated as the dynamic pressure of a liquid helium flow impinging the tweezers in transverse direction at a velocity $U=0.1 m/s$, that is 10% of the typical longitudinal flow velocity of $1 m/s$. The dynamic pressure P is taken as:

$$P = \frac{1}{2} \rho U^2$$

where the liquid helium density is $\rho \simeq 140 kg/m^3$. According to Euler-Bernoulli beam theory, the free end deflection δ_{max} of the cantilever is:

$$\delta_{max} = \frac{3}{2} \frac{Pt^4}{E_{Si}.e^3}$$

The total deflection (arm and tip) is upper-bounded by considering the sum of the deflection of a 2.5mm long tip and a 15mm (not 12.5mm) long arm. This way, the small angle generated on the tip by the arm deflection is taken into account. Using the values $t = 15mm$ (length), $e = 172\mu m$ (thickness) and $E = 140GPa$ (Young modulus), the deflection of the arm endpoint is found to be 75nm. The deflection of the tip endpoint with $t = 2.5mm$ and $e = 20\mu m$ gives a 37nm deflection. Thus, the total mechanical deflection of the tweezers tip due to a steady lateral flow of $0.1 m/s$ is a fraction of a micron, that is decades smaller than the inter-plate distance.

The mechanical resonance of the tweezers arm and tip, discussed above, could lead to deflections larger than the one due to a steady forcing. The amplitude of those mechanical oscillations was measured in a turbulent He-II flow up to velocities exceeding $1 m/s$, taking advantage of the dependence of the second sound resonance

with respect to the cavity gap. The measured signal will be presented to illustrate the efficiency of the elliptic projection method in separating the fluctuations of the acoustical path of the cavity and fluctuations of the bulk attenuation of second sound between plates. The mechanical oscillations of the cavity gap are found to be typically $0.5 \mu\text{m}$ (around 1 kHz). As expected, such a deflection is decades lower than the interplate distance (1.3 mm in this case) and than the second sound wavelength.

Boundary layer. In the presence of a mean flow through the cavity, a velocity boundary layer will develop along each tweezers plate. In principle, this boundary layer could contribute to the measured signal and therefore alter the measurement of the incoming flow, for instance by increasing the density of superfluid vortices in the cavity and therefore second sound attenuation. As illustrated later, the second sound standing wave that settles between the plates have nodes of velocity near the plates (e.g. see fig. 10 and fig. 16) while the sensitivity of second sound to vortices arises in antinodal regions of velocity. As long as the boundary layer thickness is thin enough, say within a fraction of $\lambda/4$ ($\lambda = c_2/f$ is the second sound wavelength), it is not expected to alter significantly the measured signal.

A first requirement for this condition is that the mean flow direction is parallel to the plates so that the flow penetrates through the cavity with minimal deflection. A consequence is that plates should be widely separated when operated in flows with undefined or zero mean velocity, such as the core of a mixing layer.

A second requirement is that the plate thickness is much thinner than $\lambda/4$. Present plates are 20 microns thin, to be compared with $\lambda/4 \simeq D/2n$ for the n^{th} mode of resonance. For instance, with $D = 500 \mu\text{m}$ and $n = 3$, the condition $20 \ll \lambda/4 \simeq 83 \mu\text{m}$ is indeed well satisfied.

A third condition regards the downstream development of the boundary layer thickness, which should also stay well within $\lambda/4$. The physics of boundary layers in He-II is ill-understood [SPB17] but existing experiments (e.g. see [SHVS99]) suggests that classical hydrodynamics phenomenology could remain valid in the high temperature limit. In classical hydrodynamics, the so-called *displacement* thickness of a laminar “Blasius” boundary layer at distance L from its origin is given by

$$\delta_{\text{bl}} = 1.73 \sqrt{\frac{L\nu}{U}}$$

where U is the mean velocity far from the boundary layer and ν is the kinematic viscosity of the fluid. In He-II, several diffusive coefficients could arguably play the role of ν , in particular the quantum of circulation around a quantum vortex and the kinematic viscosity associated with the dynamics viscosity of the normal fluid normalized either by the normal fluid density or by the total density. In the temperature range of interest, all these diffusive coefficients are within one order of magnitude, typ. $10^{-8} - 10^{-7} \text{m}^2/\text{s}$. Taking $\nu = 3.10^{-8} \text{m}^2/\text{s}$, $L = 1000 \mu\text{m}$ and $U = 0.5 \text{m/s}$, one finds $\delta_{\text{bl}} = 13 \mu\text{m}$, and a boundary layer Reynolds number $\delta_{\text{bl}}U/\nu = 217$ consistent with the laminar picture. This thickness estimate, similar in magnitude with the plate thickness, satisfies the third requirement $\delta_{\text{bl}} \ll \lambda/4$.

2.2 Second sound detection and generation

2.2.1 Thermometry

The temperature-sensitive material used in the present study is AuSn, which fulfills two requirements: (1) it is compatible with the microfabrication process and (2) it can be tuned to become temperature-sensitive over a range of special interest to quantum turbulence studies [WVR21], from 1.5 K up to the superfluid transition temperature $T_\lambda \simeq 2.18\text{K}$ in saturated vapor conditions. Surely, other materials would be more appropriate in other conditions, e.g. Al has been used previously for the tweezers operated around 1.5 K in [RDD⁺07].

The gold-tin AuSn thermometer is a metal-superconductor composite material, with superconducting Sn islands electrically connected by a gold layer. This granular structure is imaged by electronic microscopy in Fig.5 (right). The temperature dependence phenomenology can be interpreted in a simple way. Indeed, by proximity effect, the gold in contact with tin behaves as a superconductor over a spatial extent which depends on temperature : by adjusting the characteristic length scales and thicknesses of the granular pattern, the temperature response of the material can be tuned.

As a preliminary study, the temperature of the resistance of a 100 squares long AuSn track was tested for three different tin thicknesses, as illustrated on the left plot of Fig.6. A description of the conduction mechanism in AuSn is presented in [BSS83].

In the present study, AuSn layers are deposited by evaporation with successively a small erosion of the substrate by argon ion bombardment during 20s then the deposition of a 25nm gold layer and a 100nm tin layer (hypothetic thickness for a planar - not granular - layer). The thermometer is shaped into a meander deposited by lithographic technique on the tip of tweezers arm, as pictured in Fig.5 (right plot). The total resistance at superfluid temperatures doesn’t exceed a few hundreds of ohm, a value chosen to be much larger than the resistance of the leads but small enough to prevent parasitic effect from the leads’ capacitance (typ. few hundreds of picoFarads) up to the highest frequencies of operation.

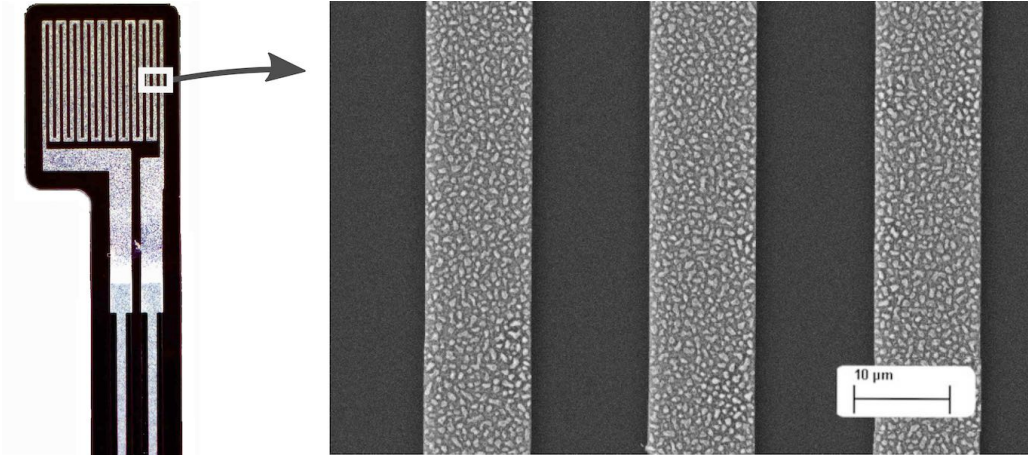


Figure 5: **Left:** Tip of tweezers arm as seen from the facing arm. The thin meander on the top is the active heater (Pt) or thermometer (AuSn). The overlap with gold tracks is apparent on the lower part of the picture **Right:** Close up picture by electronic microscopy of the AuSn thermometer showing its granular aspect. Depending on tweezers models (see fig. 8), the width of the AuSn track is 4, 11 or 24 μm

In order to obtain resistance values in this range, the meander length was fixed close to 700 squares for all tip sizes. According to the tip size, the track width was adapted so as the serpentine shape occupy the whole available area on the tip. At ambient temperature, the AuSn layer resistance was found to drift from low values to their final values during a few days (less than one week) after deposition. After this period, the resistance was found to be stable at least over 6 months.

Figure 6 (right plot) shows a typical AuSn thermometer resistance $R(T_0)$ versus temperature T_0 for different direct current I . Regarding the temperature dependence of resistance, the current density is a more determining parameter than the total current. Thus, the comparison between left and right plots of figure 6 should be done at constant values of the ratio of current over track width. At low current density ($I \lesssim 10 \mu A$), the sensitivity exceeds $1 \Omega.mK^{-1}$. At larger current densities, the current-induced magnetic field significantly shifts the superconducting-metal transition to lower temperature and broaden it, allowing to extend the measurement range down to 1.6 K and below. In the range of currents explored in Fig. 6, the reduction of sensitivity in $\Omega.K^{-1}$ at larger current I is more than compensated by the larger sensitivity in $V.K^{-1}$ units across the thermistor. Most measurements presented hereafter are done with a polarization of $I \simeq 27 \mu A$.

2.2.2 Heating

The heater consists in a meander of metal deposited by lithographic technique on the tip of a cantilever, alike the thermometer (see fig. 5 (left)). The same lithographic mask was used, and therefore the meander length is also close to 700 squares for all the tip sizes.

As can be seen on figures 4 and 5, a buffer zone was designed between the gold tracks and the meander. Into this zone, the electrical path is wide but the material is the same as in the meander (platinum for heater). The buffer zone length is approximately 20 squares. This design aims at providing some thermal isolation between the meander and the gold track.

Numerous resistive materials are suitable, e.g. chrome was used for the tweezers in [RDD⁺07] and platinum in [WVR21]. Present data have been obtained with platinum to benefit from the temperature-independence of its resistivity at superfluid temperatures [PK82], and nevertheless to allow re-use of these miniature heaters as miniature thermometers or hot-film anemometers in experiments conducted at higher temperatures where Pt regains temperature dependence [Kem91]. A 5nm titanium layer was deposited prior to platinum as an adhesion layer.

The thickness of the Pt layer, around 80 nm, was chosen such that the electrical resistance of the heater at superfluid temperature is around a few hundreds of ohms, like for the thermometer maximum resistance and for the same reasons.

The heater is driven with a sinusoidal current at frequency $f/2$. The resulting Joule effect can be decomposed into a constant mean heating and the sinusoidal heat flux at the frequency f that drives the second sound resonance. A benefit of this $f/2$ excitation is that the signal monitored by the thermometer - centered around f - is not spoiled by spurious sub-harmonic electromagnetic coupling at $f/2$ from the excitation circuitry. Thus, no special care is needed to minimize the electromagnetic cross-talk between the electrical tracks of the heater and the electrical tracks of the thermometer, despite their proximity.

The non-zero mean heating results is a steady thermal flux in He-II, the corresponding entropy being carried

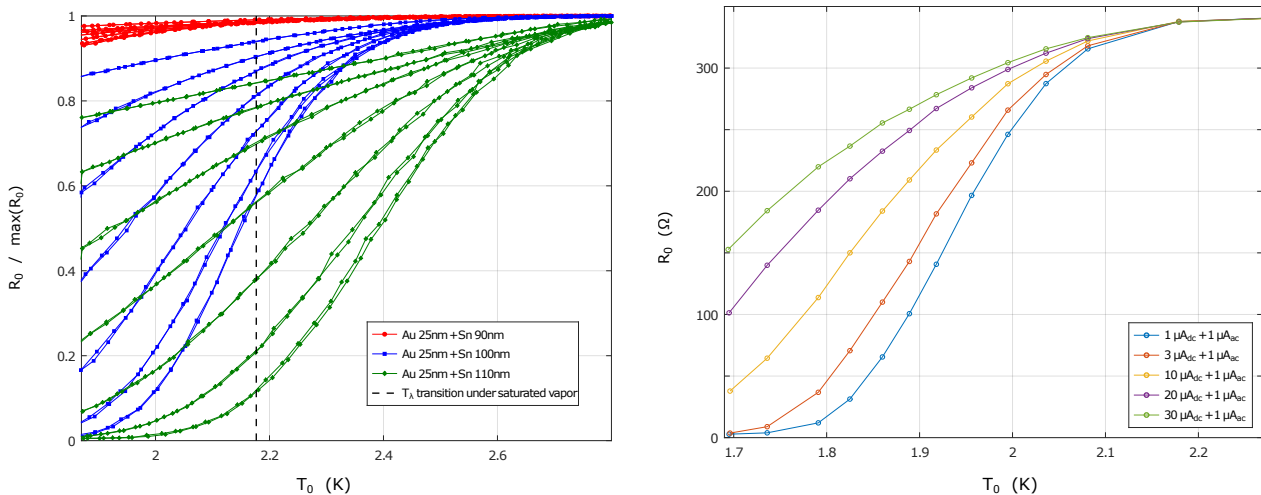


Figure 6: **Left:** Example of temperature and current dependence of AuSn layers with different Sn thicknesses deposited on a track of width $50\mu\text{m}$. The current polarization spans from $1\mu\text{A}$ up to 1mA . **Right:** Temperature response of the AuSn track of small tweezers for different electrical currents. The thickness of the tin layer is 100 nm of Tin, and the width of the track is $4\mu\text{m}$. The small difference between both plots -when compared at similar current densities- is compatible with the uncertainty on the layer thicknesses. This good agreement indicates that AuSn properties are robust to the full fabrication process of the tweezers. No significant aging of AuSn properties has been noticed over a few years period.

away from the heater in the form of steady normal fluid flow. This outgoing normal flow is balanced by an opposite steady mass flow of superfluid towards the heater. Such cross-flows are referred to as *counterflows* in the quantum fluid literature[Tou82, NF95]. This steady counterflow adds up to a pure second sound generated by the heater, but -contrary to it- its effects are not amplified by resonance in the cavity.

Quasi-linear vs non-linear regimes. The second sound resonators are operated with standing waves of low amplitude, say $\sim 100\mu\text{K}$. In this limit, the amplitude T of the temperature standing wave nearly responds linearly to the heating power P . For larger heating power, the ratio T/P decreases with P , which is interpreted as the result of a turbulent transition within the tweezers which fuels a dense tangle of quantum vortices dissipating the second sound wave³. The crossover from the quasi-linear to non-linear response of $T(P)$ is illustrated by figure 7 (left plot) for tweezers at 1.6 K in the absence of external flow. In these conditions and for these tweezers, the transition occurs around $P \simeq 1\text{ W/cm}^2$, where P is the total Joule power normalized by the heating surface. In other conditions, this transition was observed at smaller power densities, but no systematic study was carried on the threshold value.

2.2.3 Digression on the operation in the non-linear heating regime

The present study focuses on the linear regime of heating, but a short digression on higher powers allows uncovering a noteworthy property of non-linear operation and incidentally backing-up the above interpretations of the nature of the non-linear regime. Figure 7-right displays the amplitude of the (normalized) temperature standing wave T/P versus P in flows of different mean velocities U and turbulence intensity of few percents. In the linear regime ($P \lesssim 1\text{ W/cm}^2$ in the conditions of Fig. 7), the plateaus of T/P decreases when U increases. Following the classical interpretation (see later), the standing wave T is damped by the vortices present in the external flow, which concentration increases with U . Interestingly, in the non-linear regime (say for $P \gtrsim 2\text{ W/cm}^2$ in Fig. 7), the dependence of T/P versus U is opposite. The interpretation is that the extra damping of the

³In one dataset, a close look at the quasi-linear region in quiescent superfluid around 1.5 K evidenced a small discontinuity of T/P versus P dependence around $P^* \simeq 10^{-2}\text{ W/cm}^2$ (not shown), suggesting another flow transition, but this small effect was not detectable in other datasets. A Reynolds number of this possible transition can be defined with the transverse characteristic length scale $L \simeq 1\text{ mm}$, the quantum of circulation $\kappa \simeq 0.997 \cdot 10^{-7}\text{ m}^2/\text{s}$ and the counterflow superfluid velocity towards the heater $v_s \simeq 0.3\text{ mm/s}$ (amplification of velocity by the quality factor of the cavity has not been taken into account). One finds $Re_s = v_s L / \kappa \simeq 3$. Critical Reynolds numbers Re_s of a few units have already been reported to characterize the threshold of appearance of a few superfluid vortices across the section of pipes that are closed at one of their ends with a heating plug (see fig. 3 in [BLR17]), a transition referred as the T1-transition in the counterflow literature [Tou82, NF95]. By analogy, this could suggest that the discontinuity at P^* might be associated with the appearance of a sparse tangle of the quantum vortices near the heater, which density is expected to increase for larger P . Such vortices would damp the standing wave, but no such effect has been detected. Indeed, first the observed damping of the standing wave in quiescent He-II can be accounted for by the sole effect of diffraction (as shown later), which indicates that all the other sources of loss are comparatively small. Second, loss due to such “counterflow” vortices would make the $T(P)$ dependence sub-linear rather than linear, which is not clearly observed. Since no quantitative evidence of these vortices could be clearly identified, this effect was not further explored.

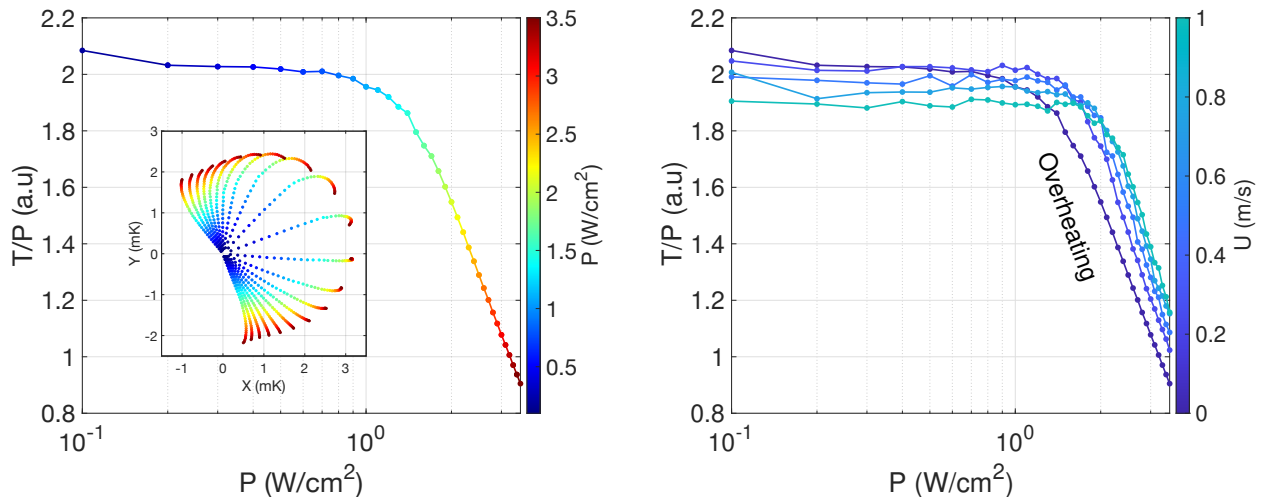


Figure 7: **Left:** Normalized amplitude T of the temperature standing wave versus heating power P for second sound tweezers in a quiescent He-II around 1.6 K. The transition around $P = 1 \text{ W/cm}^2$ is interpreted by the development of a self-sustained vortex tangle within the probe. The insert shows the amplitude of the temperature standing waves in the complex plane for a subset of frequencies belonging to the same second sound resonance. In this representation, the extra-dissipation associated with the self-sustained vortex tangle results in a curvature of the iso-frequency radial “lines” revealing the broadening of the resonance. **Right:** Same quantity for second sound tweezers swept by turbulent flows of different mean velocities but similar turbulence intensity. In the linear regime $P \lesssim 1 \text{ W/cm}^2$, the velocity dependence is opposite to the one in the non-linear regime, $P \gtrsim 2 \text{ W/cm}^2$, demonstrating respectively vortex and velocity sensing by the probe.

standing wave T now mostly results from the vortices generated within the tweezers by the heating itself. This vortex density decreases at larger U because vortices are more efficiently swept out of the tweezers. In the non-linear regime, the second-sound tweezers thus behave as a local anemometer. In the linear regime, we will show that second-sound tweezers can not only behave as vortex probes -as illustrated by Fig.7-right but also as anemometers through a mechanism discussed later.

2.3 Microfabrication and assembling

Mechanical and electrical assembly.

The distance between the plates is set by the spacer, composed of one or several micro-machined silicon elements. Additionally, two Kapton films with golden copper tracks are inserted in contact with the gold tracks of the heater and thermometer. The cantilevers, Kapton films and spacer elements are stacked on each other as shown in Fig.3. The resulting assembly is clamped with a standard picture clip, downsized by electro-wire erosion, and soldered to the head of a mounting screw. An improvement compared to the clamping technique introduced in [RDD⁺07] is the possibility to insert a temporary “joystick” through the whole assembly to allow precise alignment (or offsetting) of the cavity plates under microscope (see Fig.2-a).

All the mechanical structures of cantilevers and spacers are made of silicon. The cantilevers are fabricated by processing SOI (Silicon On Insulator) substrates by microelectronic techniques. The substrates diameter is 100mm, the silicon substrate, oxide and device thicknesses are respectively 500 μm , 1 μm and 20 μm . The substrates are double side polished. The wafers are oxidized so as to form a 100nm thick SiO₂ layer on both sides. Distinct wafers are used to fabricate heaters and thermometers but the process differs only in the metals used for tips electrical paths. By using a circular symmetry design, 46 cantilevers are made per wafer.

The cantilevers’ fabrication process is presented in table 1. The serpentine electrical path (red color) is deposited first on the SOI wafer frontside. The deposition is done using standard photolithography, evaporation and lift-off sequence. The photoresist used is AZ 5214E from Microchemicals GmbH, processed as a negative photoresist. Depending on the cantilever type, heater or thermometer, two different evaporation sequences are used: Ti 5nm + Pt 80nm or Au 25nm + Sn 100nm. Evaporation is preceded by in situ wafer surface cleaning by an argon ions bombardment during 20s. Lift-off is initiated in an acetone bath during 5min and then completed by ultrasounds during a few tens of seconds. The current leads (orange color) are deposited during a second photolithography, evaporation and lift-off sequence. The evaporation sequence is Ti 5nm + Au 200nm + Ti 5nm + Pt 50nm. The usage of a platinum layer was found to facilitate lift-off and may also be useful for brazing purpose. A thin protective resist layer is deposited on frontside in order to protect it during all subsequent operations on the backside.

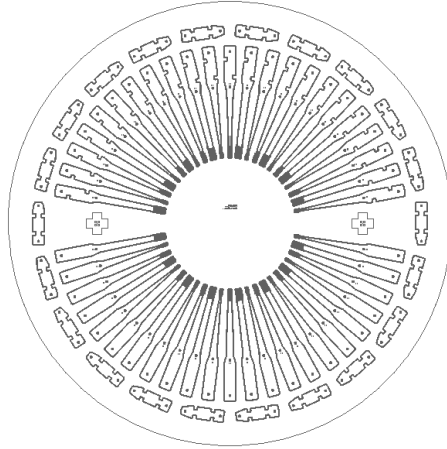


Figure 8: Overview of mask design (the disk diameter is 100mm).






Side	Step	Surface material	Design
Frontside	1. Electrical circuitry fabrication.	TiAuTiPt (orange) AuSn/TiPt (red)	
Backside	2. Aluminum mask fabrication.	Aluminum	
Backside	3. Resist mask fabrication. 4. Etching of surface oxide and silicon. 5. Resist removal.	Photoresist	
Backside	6. Etching of surface oxide and silicon until buried oxide is reached. 7. Etching of buried oxide. 8. Aluminum removal.	Aluminum	
Frontside	9. Resist mask fabrication. 10. Etching of surface oxide and silicon until opening.	Photoresist	

Table 1: Cantilevers fabrication process.

Phase	Deposition		Etch	
Sub-phase	Main	Boost	Main	
Gas	C ₄ F ₈ : 250 sccm	SF ₆ : 250 sccm O ₂ : 45 sccm	SF ₆ : 450 sccm O ₂ : 45 sccm	
Duration	2.2 s	2.0 s	5.5 s	
Pressure	14 mTor	20 mTor	75 mTor	
Coil power	1200 W	1780 W	1780 W	
Platen power	20 W	110 W	50 W	
Electromagnet current	0 A	0 A	2 A	
Platen frequency	RF 13.56 MHz			
He backside pressure	10 Tor			

Table 2: Bosch process recipe used during deep silicon etching on backside.

The cantilevers 3D structuration starts with a backside deep etching of silicon. Two superimposed etch masks are fabricated first, one aluminum mask and one photoresist mask deposited over the aluminum one. The aluminum mask is made in the same way as the frontside electrical paths. A backside alignment is necessary during photolithography. The aluminum thickness is 120nm. The protective resist layer on frontside had to be deposited again after lift-off. The resist mask is made by photolithography on the positive AZ4562 photoresist spin-coated at 4000rpm. The aluminum mask is identical to the resist mask except within the arm area, as shown in table 1. This area is covered by resist but not by aluminum. Thus, the resist fully covers aluminum.

After the fabrication of both masks, the deep etching is started, with the resist mask protecting both silicon oxide and aluminum surfaces. The surface oxide is etched first then the solid silicon. The thin oxide layer is etched by reactive ion etching (RIE) based on SF₆ gas. The silicon was etched in a STS HRM deep reactive ion etching (DRIE) equipment using a recipe based on Bosch process. The recipe is presented on table 2, the etch duration is 120 cycles. As shown on table 1, a 200µm wide trench is dug from the backside around the baseplate and arm areas. The tip area is fully exposed to etching as this part was extracted from the device layer of SOI only. The longer this phase, the thicker the cantilever arm at the end of process.

Following this first etch phase, the resist is removed by an oxygen plasma and the backside surface oxide is etched into the freshly uncovered arm area. Then, another silicon etch sequence is applied with the remaining aluminum mask. Its objective was to thin the arm and to reach the buried oxide of SOI in the trench, at the same time. The same recipe is used, 200 cycles are applied. The Bosch process is interrupted 3 times, every 50 cycles, in order to apply a 1min oxygen plasma followed by 20s of an isotropic silicon etching recipe (plasma pressure 75mTor, SF₆ flow 450sccm, O₂ flow 45sccm, coil power 1780W, platen power 50W). The objective is to reduce the parasitic effect generated by the passivation layer deposited on arm sidewalls during the first deep silicon etching sequence. As the arm area is masked during the first silicon etch sequence and unmasked during the second one, the passivation layer located along the arm edges is released and could generate locally some irregular micromasking effect. The oxygen plasma is intended to help remove the floating passivation films. The isotropic silicon etching is intended to cut the silicon pillars generated by micromasking. The final 50 cycles of the Bosch process recipe end up reaching the SOI buried oxide layer, at the trench bottom, all around the cantilever (however the oxide should not be reached into the arm area). It is necessary at this step to check that the buried oxide is fully uncovered by silicon everywhere in the trench bottom and in the tip area. However, etching cycles should not be applied in excess so as to avoid some mechanical weakening of the wafer. At this step, the arm thickness has its final value. The buried oxide is then removed by plasma etching. This oxide is fully removed at the trench bottom and in the tip area. If this layer is not removed, some bending may occur on the tip at the end of process, due to mechanical stress of oxide. The aluminum mask is removed in an aluminum etchant solution at 50°C during a few minutes. The frontside protective resist layer is removed during an acetone cleaning bath.

The 3D cantilever structuration is ended by a third silicon etching made from the frontside. The etch mask is formed by photolithography on AZ1512HS resist, deposited at 4000rpm. As shown on table 1, the mask design includes two bridges on the baseplate sides in order to maintain the cantilever after having opened the trench that surrounds it. The design also includes the tip contour. The frontside thin surface oxide is etched first, then the silicon of the device layer. The silicon etching is done with specific conditions. Due to the wafer mechanical weakness at this step, caused by the multiple deep trenches made on the backside, the processed wafer is layed on and attached to a blank silicon wafer by Kapton tape. This ensemble is loaded into the etching chamber. As no thermal bridge is present between the two wafers, the recipe is adapted: low RF powers are used and a 22s idle time is added after each etching cycle (see table 3). The objective is to avoid overheating during etching. The silicon etch duration is 50 cycles.

After this sequence, the trench around cantilever is fully opened. The resist is removed by a low power oxygen plasma. Some spacers are fabricated together with the cantilevers but most of them are made separately from

Phase	Deposition	Etch		
Sub-phase	Main	Delay	Boost	Main
Gas	C ₄ F ₈ : 250 sccm	SF ₆ : 250 sccm O ₂ : 10 sccm		
Duration	3 s	2.0 s	5.5 s	22.5 s
Pressure	14 mTor	20 mTor	40 mTor	40 mTor
Coil power	300 W	300 W	300 W	1 W
Platen power	20 W	100 W	50 W	1 W
Electromagnet current	0 A	0 A	2 A	0 A
Platen frequency	RF 13.56 MHz			
He backside pressure	10 Tor			

Table 3: Bosch process recipe used during deep silicon etching on frontside.

two silicon wafers with thicknesses 300 μ m and 525 μ m. These wafers are covered by thin dielectric layers on both sides.

2.4 Electric circuit

Figure 9 shows a circuit used for time-resolved measurements with second-sound tweezers, with example values of resistances and gain. The time-resolved data presented in this paper have been obtained with such a circuit and using the following equipment. The front-end of the preamplifier is the EPC1-B model by Celian or an SA-400F3 model by NF when frequencies above 100 kHz are explored. The lock-in amplifier is a LI-5640 by NF or Model 7280 by SignalRecovery above 100 kHz. In most conditions, its built-in internal generator provides both the drive of the tweezers heater (at frequency $f/2$) and the reference frequency to detect the temperature signal (at frequency f). The acquisition system is built around PXI-4462 analog input cards by National Instrument, and it records both the in-phase (X) and quadrature (Y) signal from the analog outputs of the lock-in amplifier.

In occasional conditions, the temperature signal at the lock-in input is buried in a much larger electromagnetic parasitic signal at $f/2$, and it cannot be properly resolved by the limited voltage dynamic range of the lock-in amplifier. This situation can occur when the tweezers are operated far from a resonance, where the second sound signal is small, or when the tweezers are operated at very high frequency (say > 100 kHz), as electromagnetic coupling increases with frequency. The magnitude of this parasitic coupling depends on the geometrical and electrical specificities of the tweezers and cables. In the range of parameters explored in the present study, the order of magnitude of the parasitic voltage induced across the thermometer resistor, normalized by the voltage applied across the heating resistor, is

$$0.5\% \times \frac{f/2}{100kHz}$$

Such situations are handled thanks to the differential input of the lock-in amplifier, by removing a signal mimicking the parasitic one. In such cases, a two-channel waveform generator is used: one channel driving the heater (at frequency $f/2$), another channel mimicking the parasitic signal (at frequency $f/2$, with manually tuned amplitude and phase shift) and the "sync" output of the generator synchronizing the lock-in demodulation (at frequency f). The 33612A generator by Agilent is used for this purpose. Alternatively, the compensation signal can be generated directly from the lock-in internal generator, completed with a simple RC phase shifter and eventually ratio transformer.

In principle, any positive temperature coefficient thermistor-like AuSn thermometer- that is not well thermalized with the fluid can become unstable when driven by a current source. Indeed, an infinitesimal thermistor fluctuation from T_0 to $T_0 + \delta T_0$ entails a resistance variation of $\delta R = \partial R / \partial T_0 \cdot \delta T_0 > 0$, leading to an excess of Joule dissipation $\delta R \cdot I^2$ for a constant current drive I . Calling \mathcal{R}_{th} is the thermal resistance of the thermistor-fluid interface, this extra Joule dissipation results in an overheating $\mathcal{R}_{th} \times \delta R \cdot I^2$ which could lead to a thermal instability. The stability condition is difficult to predict for spatially distributed thermistor deposited on a Si crystal and immersed in superfluid. Thus, first tests have been done with a voltage polarization, before validating empirically the stability of our current polarization.

The frequency bandwidth of the measurements is arbitrarily set by the integration time constant of the lock-in amplifier. In practice, the performance of the circuit are limited by the $0.65 nV/\sqrt{Hz}$ input voltage noise of the EPC1-B pre-amplifier, all other sources of noise being smaller. For a $27 \mu A$ current polarization, a thermometer sensitivity of $0.5 \Omega \cdot mK^{-1}$, and a 10 Hz or 1000 Hz bandwidth of demodulation, the temperature resolution T_{rms} is :

$$T_{rms} = \frac{\sqrt{10} \cdot 0.65}{0.5 \times 27} \mu K \simeq 150 nK \text{ for a 10 Hz measurement bandwidth}$$

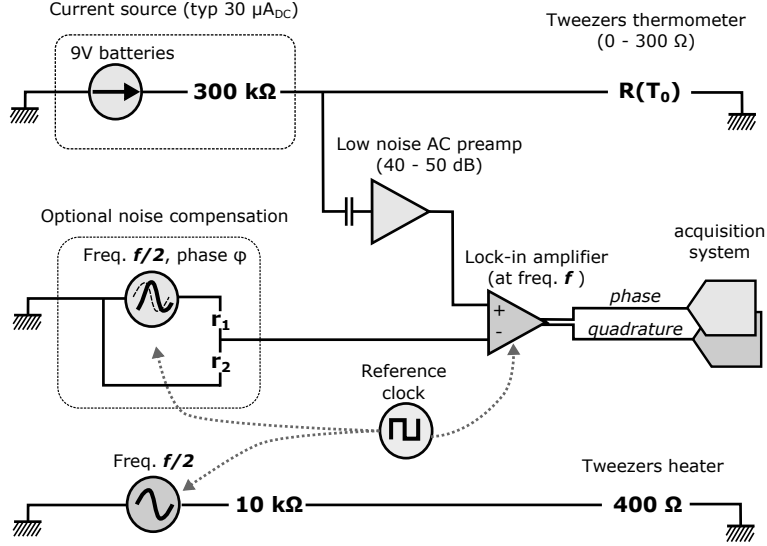


Figure 9: Example of circuitry for measurements with a high dynamical reserve.

or

$$T_{rms} = \frac{\sqrt{1000} \cdot 0.65}{0.5 \times 27} \mu K \simeq 1.5 \mu K \quad \text{for a 1 kHz measurement bandwidth}$$

These resolutions are sufficient in standard conditions. Indeed, they are respectively 3 and 2 decades smaller than the typical amplitude of a second sound at resonance, and reaching the same temperature resolution at significantly larger bandwidth would be useless given the space-time resolution of the probe itself. If needed, better resolution could nevertheless be achieved with a larger polarization across the thermometer or using a cryogenic amplifier (e.g. see [DLF⁺14] and <http://cryohemt.com>) before being limited by the thermal noise floor of the thermistor (typ. $0.15 \text{ nV}/\sqrt{\text{Hz}}$ for 200Ω at 2 K).

3 Models of second sound resonators

The second sound equations within the linear approximation can be written in terms of the temperature fluctuations T and the velocity of the normal component \mathbf{v}_n as

$$\begin{aligned} \partial_t \mathbf{v}_n + \frac{\sigma \rho_s}{\rho_n} \nabla T &= 0, \\ \partial_t T + \frac{\sigma T_0}{c_p} \nabla \cdot \mathbf{v}_n &= 0. \end{aligned} \quad (1)$$

with σ the entropy per unit of mass, c_p the heat capacity, and ρ_s , ρ_n are the densities of the superfluid and normal components respectively. All along the present section, T_0 is the notation for the bath mean temperature whereas T denotes the temperature fluctuations, with $\langle T \rangle = 0$.

We introduce the second sound velocity c_2 defined by the relation

$$c_2^2 = \frac{\rho_s}{\rho_n} \frac{\sigma^2 T_0}{c_p}. \quad (2)$$

It can be deduced from Eqs. (1) that both the temperature T and the normal velocity \mathbf{v}_n follow the wave equation

$$\partial_t^2 T - c_2^2 \Delta T = 0. \quad (3)$$

We explain in the present section how Eqs. (1-2-3) can be used to build quantitative models of second sound resonators. We first focus on phenomenological aspects in sec. 3.1. Then, we give analytical approximations in sec. 3.2 and an accurate numerical model in sec. 3.3. Finally, we discuss the model quantitative predictions in secs. 3.4 and 3.5.

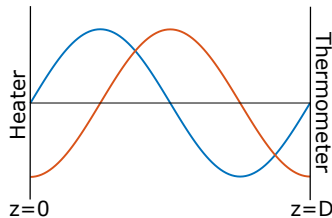


Figure 10: Schematic representation of the second resonant mode of a second sound cavity. The red curve displays the temperature field at time $t = 0$, and the blue curve displays the normal fluid velocity v_n at time $t = \frac{1}{4f}$, where f is the excitation frequency.

3.1 Resonant spectrum of second sound resonator: phenomenological aspects

The basic idea of second sound resonators is to create a second sound resonance between two parallel plates facing each other. A second sound wave is excited with a first plate, while the magnitude and phase of the temperature oscillation is recorded with the second plate used as a thermometer (see Fig. 10). For simplicity, we assume from now on that the second sound wave is excited by a heating, but the whole discussion can be straightforwardly extended to nucleopore mechanized resonators. The temperature oscillations within the cavity are coupled to normal fluid velocity oscillations according to the second sound equations (1). Both components oscillate in quadrature, which means that they reach their maximal amplitude with a $\frac{1}{4f}$ time shift (Fig. 10).

We note $j_Q = j_0 e^{2i\pi f t}$ the periodic component of the heat flux emitted from the heater. We assume throughout the present article perfectly insulating plates, which means that the boundary conditions for the second sound wave are

$$\mathbf{v}_n \cdot \mathbf{n} = \begin{cases} 0 & \text{for } z = D \\ \frac{j_Q}{\rho \sigma T_0} & \text{for } z = 0 \end{cases}, \quad (4)$$

where \mathbf{n} is the unit vector directed inward the cavity and normal to the plates. The second equation in (4) reflects the fact that the normal component carries all the entropy in the fluid. As illustrated in Fig. 10, the thermometer plate is a node of the normal velocity oscillation, whereas the normal velocity amplitude only vanishes on the heater plate in quadrature ($t = \frac{1}{4f} + \frac{n}{2f}$). According to the first relation in Eq. (1), the boundary conditions (4) for the normal velocity translate into the following boundary conditions for the temperature field

$$\nabla T \cdot \mathbf{n} = \begin{cases} 0 & \text{for } z = D \\ -\frac{\rho_n \partial_t j_Q}{\rho \rho_s \sigma^2 T_0} & \text{for } z = 0 \end{cases}. \quad (5)$$

In particular, the thermometer plate is an antinode for the temperature.

We display in Fig. 11 a typical experimental spectrum of second sound tweezers, that is, the temperature magnitude averaged over the thermometer plate, as a function of the heating frequency f . The spectrum is reminiscent of a Fabry–Perot resonator (described in sec. 3.2): it displays very clear resonant peaks almost equally separated, and a stable non-zero minimum at the non-resonant frequencies. However, the spectrum of Fig. 11 displays three major characteristics that can be observed for every tweezers spectrum. First, the location of the resonant frequencies are slightly shifted compared to the standard values f_n given by $\frac{2\pi f_n D}{c_2} = n\pi$, ($n \in \mathbb{N}$) expected for an ideal Fabry–Perot resonator. Only for large mode numbers do the resonant peaks again coincide with the expected values. Second, the temperature magnitude vanishes in the zero frequency limit, and the first modes of the spectrum grow linearly with f . In between, the resonant amplitudes saturate and then slowly decrease at high frequency.

These latter peculiarities of the frequency response were not described in previous references about second sound resonators. This prompted us to study different models for second sound resonators, including the finite size effects and near field diffraction phenomena. We first describe analytical approximations in sec. 3.2, then we develop in sec. 3.3 a numerical algorithm based on the exact solution of the wave equation (3). The numerical scheme can be adapted for various types of planar second sound resonators. We then give quantitative predictions specifically for the response of second sound tweezers without and in the presence of a flow in sec. 3.4 and a summary of the main results in sec. 3.5.

3.2 Analytical approximations

The starting point to build our model of second sound tweezers is to assume that all zeroth order physical effects observed with the tweezers are geometrical effects of diffraction. This means in particular that we assume perfectly reflecting resonator plates, and we also neglect bulk attenuation of second sound waves when

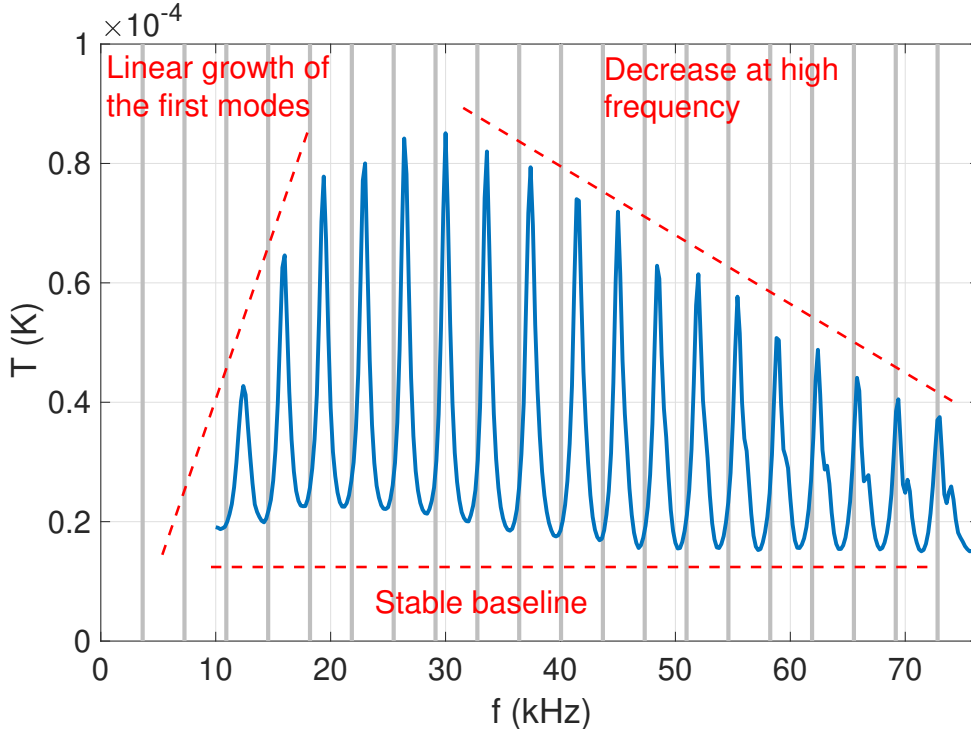


Figure 11: Experimental spectrum of second sound tweezers of lateral size $L = 1$ mm and gap $D \approx 1.435$ mm. f is the heating frequency, and T is the thermal wave magnitude. The figure displays the main characteristics of tweezers typical spectrum: first, the resonant frequencies are not located at the values f_n given by $\frac{2\pi f_n D}{c_2} = n\pi$, ($n \in \mathbb{N}$), displayed by the gray vertical lines. The amplitudes of the resonant modes first increases linearly with f until they saturate and eventually decrease at high frequency. The baseline level only weakly depends on f .

the fluid is at rest [CR83, RG84]. These assumptions turn to be self-consistent, because the predictions of the model developed in sec. 3.3 reproduce the main features observed in experiments. We thus start with the simplest model of a resonant cavity for planar waves, namely the Fabry–Perot model. We then propose variations of the Fabry–Perot model, taking progressively into account the particular resonator geometry. We discuss the predictions of these models and their relevance for our second sound tweezers.

The standard Fabry–Perot model The Fabry–Perot model corresponds to a one-dimensional resonator composed of two infinite parallel plates separated by a gap D . In that case, the wave Eq. (3) together with the boundary conditions Eqs. (5) can be solved exactly, for a periodic heating $j_Q = j_0 e^{2i\pi f t}$. However, as there is no energy loss between two perfectly insulating and infinite plates, a bulk dissipation has to be introduced by hand in the model, to balance energy injection from the heater. This can be done with an additional dissipation coefficient ξ (in m^{-1}). The temperature at the thermometer plate is $T(t) = \mathcal{R}e(\bar{T} e^{2i\pi f t})$ (where $\mathcal{R}e$ is the real part operator) with the complex wave amplitude \bar{T} given by

$$\bar{T} = \frac{A}{\sinh\left(i\frac{2\pi f D}{c_2} + \xi D\right)}, \quad (6)$$

with $A = -\frac{j_0}{\rho c_p c_2}$. An illustration of a Fabry–Perot spectrum is displayed in grey in Fig. 14, with $\xi D = 0.15$ and $A = 1$. We introduce the wave number $k = \frac{2\pi f}{c_2}$. It can be proved from Eq. (6) that the spectrum maxima are reached for the values $k_n D = n\pi$, ($n \in \mathbb{N}$), and correspond to constructive interferences in the cavity. The baseline level is set by the minima reached for the values $k_n D = n\pi + \frac{\pi}{2}$, ($n \in \mathbb{N}$), and correspond to destructive interferences in the cavity. For the simple Fabry–Perot model of Eq. (6), all the resonant peaks have equal height and are uniformly separated. Therefore, some main features of experimental spectra are missing, an indication that important other physical effects have to be included in the model.

Second sound resonators embedded in infinite walls A possible modification of the Fabry–Perot resonator is to consider finite-size heater and thermometer of size L embedded in two parallel and infinite walls facing each other. This geometry is most commonly encountered in the literature. With such a configuration,

the thermal wave is not a plane wave any more because it is emitted by a finite size heater. The model thus contains diffraction effects, that the simplest Fabry–Perot resonator do not display. An illustration of the model setup is displayed in Fig. 12. An exact solution of the wave equation Eq. (3) can be found using the technique of image source points. Let Σ_1 be the heating plate and Σ_2 be the thermometer plate, and we assume that the thermometer is sensitive to the average temperature over Σ_2 . Then the response of the tweezers is given by $T(t) = \mathcal{R}e(\bar{T}e^{2i\pi ft})$ with

$$\bar{T} = \frac{ikj_0}{2\pi\rho c_p c_2} \frac{1}{L^2} \iint_{\Sigma_2} d^2\mathbf{r}_2 \iint_{\Sigma_1} d^2\mathbf{r}_1 G(\mathbf{r}_2 - \mathbf{r}_1),$$

with the Green function $G(\mathbf{r})$ defined for every vector \mathbf{r} in the (x, y) plane

$$G(\mathbf{r}) = 2 \sum_{n=0}^{+\infty} \frac{1}{|(2n+1)D\mathbf{e}_z + \mathbf{r}|} e^{-ik|(2n+1)D\mathbf{e}_z + \mathbf{r}|}.$$

Such a model correctly predicts that the tweezers spectrum vanishes when the heating frequency f goes to zero. Yet, it does not reproduce the linear increase of the resonant magnitude of the first modes, neither the decrease of the resonant peaks at large frequency observed in experiments with second sound tweezers. This means that other effects have to be taken into account to model a fully-immersed open resonant cavity such as non-perfect plates alignment and energy loss by diffraction outside the cavity when the latter is not embedded in infinite walls.

Empirically modified Fabry–Perot model Contrary to a Fabry–Perot resonator composed of infinite plates, second-sound resonators are built with plates of finite size L , approximately of the same order as the gap D between them. Those finite size effects are important as they introduce a frequency-dependent energy diffracted outside the cavity. This mechanism is sketched in Fig. 12. According to standard diffraction theory, a finite wave initially of size L with a wavelength $\lambda = \frac{c_2}{f}$ spreads with a typical opening angle given by $\frac{\lambda}{L}$. By this geometrical effect, a part of the wave energy is lost as the wave reaches the other side of the cavity. The energy loss is roughly proportional to the surface of the wave cross-section that “misses” the reflector (see the right panel of Fig. 12). Therefore, the fraction of energy lost at the wave reflection is controlled by the ratio

$$\begin{aligned} \frac{(L + \frac{2\lambda D}{L})^2 - L^2}{(L + \frac{2\lambda D}{L})^2} &\approx 4 \frac{\lambda D}{L^2}, \\ &\approx \frac{4}{N_F}, \end{aligned} \quad (7)$$

where we have introduced the Fresnel number $N_F = \frac{L^2}{\lambda D}$.

The tweezers plates are mounted at the top of arms of a few millimeters. The perfect parallelism of the plates is usually not reached for our tweezers, but a small inclination γ of the order of a few degrees can be observed instead. A relative inclination γ -even small- of both plates creates an additional energy loss mechanism (see Fig. 13). Intuitively, this second mechanism is controlled by the non-dimensional number

$$N_i = \frac{\lambda}{\gamma L}. \quad (8)$$

We assume that the Fabry–Perot model (6) can be corrected using the two non-dimensional numbers $N_F = \frac{L^2 f}{c_2 D}$ in Eq. (7) and $N_i = \frac{c_2}{\gamma f L}$ in Eq. (8). More precisely, based on empirical observations, we find that second-sound tweezers spectra can be accurately represented by the formula

$$\bar{T} = \frac{A}{\sinh\left(i\left(\frac{2\pi f D}{c_2} - a\frac{c_2 D}{L^2 f}\right) + b\frac{c_2 D}{L^2 f} + c\left(\frac{\gamma f L}{c_2}\right)^2\right)}, \quad (9)$$

where a, b and c are fitting coefficients. As there is no other small parameter in the problem, a reasonable assumption is to look for coefficients of order one. We find that the values $a \approx 0.95$, $b \approx 0.38$ and $c \approx 1.3$ give accurate spectra predictions. An illustration of a modified Fabry–Perot spectrum with Eq. (9) is given in Fig. 14. The linear amplitude growth of the first resonant peaks can be interpreted as a progressive focalization of the wave, and is thus controlled by the Fresnel diffraction number N_F in Eq. (12). The shift proportional to $\frac{1}{f}$ in peaks frequency positions, observed in the experimental spectra, is also controlled by N_F . The decrease in resonant magnitude for large mode numbers can be interpreted as a wave deflection outside the cavity, after back and forth propagation between the plates. This latter effect is controlled by the second non-dimensional number N_i in Eq. (8).

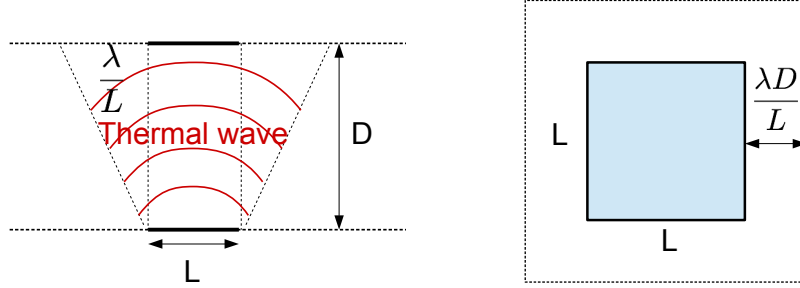


Figure 12: Representation of the wave dispersion. The energy loss is controlled by the non-dimensional number $\frac{\lambda}{L}$, according to standard diffraction theory. In this section, we discuss both the case of tweezers embedded in walls, and the case of free tweezers in open space.

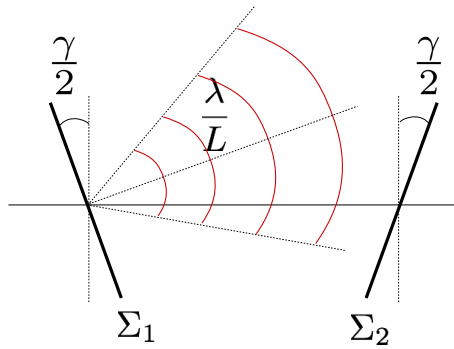


Figure 13: Effect of the plates' inclination γ . Inclination creates an additional energy loss mechanism controlled by the second non-dimensional number $\frac{\lambda}{\gamma L}$.

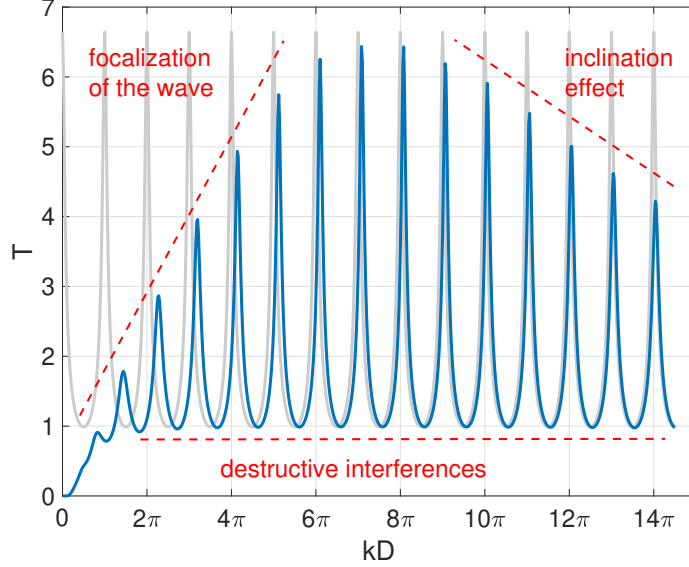


Figure 14: Analytical models of second-sound tweezers. The grey curve represents the standard Fabry-Perot spectrum. The blue curve represents the empirical correction of the Fabry-Perot formula using the two non-dimensional numbers $\frac{\lambda}{L}$ and $\frac{\lambda}{\gamma L}$. The modified spectrum displays the characteristic features of a tweezers experimental spectrum, as displayed in Fig. 11.

The major interest of the Fabry-Perot model is to offer an analytical expression to fit locally a resonant peak of second sound resonator spectrum. The local fit of a peak is of particular interest to interpret the experimental data, as will be explained in sec. 4. Based on Eq. (9), given a measured resonant frequency f_0 , we will look for a fitting expression

$$\bar{T} = \frac{A}{\sinh\left(i\frac{2\pi(f-f_0)D}{c_2} + \xi_0 D\right)}, \quad (10)$$

valid for second sound frequencies f close to f_0 . In that expression, ξ_0 encapsulates the different geometrical mechanisms responsible for energy loss when the fluid is at rest. A and ξ_0 are thus fitting parameters that can be found easily with the experimental data obtained by varying f in the vicinity of f_0 .

3.3 Numeric algorithm

Sec. 3.2 presents a class of models of increasing complexity, still with an analytical solution. Those models show how all zeroth-order effects observed with second sound resonators can be recovered from geometrical diffraction effects. However, they do not allow for quantitative *predictions* of the resonator spectra, nor do they allow including the effects of a flow. We develop in the present section a numerical algorithm, based on the exact resolution of the wave equations with the particular tweezers geometry, with and without flow. The algorithm could be extended to any second sound resonator with a planar geometry. As will become clear in the following, this numerical model allows going far beyond the approximate models of sec. 3.2.

3.3.1 For a background medium at rest

The aim of the present section is to build a numerical algorithm to solve the wave equation (3) for a periodic heating $j_Q = j_0 e^{2i\pi f t}$. We look for a solution with the ansatz $T(\mathbf{r}, t) = \mathcal{R}e(\bar{T}(\mathbf{r})e^{2i\pi f t})$. Then, the wave equation for \bar{T} is

$$\Delta \bar{T} + k^2 \bar{T} = 0,$$

where we have introduced the wave number $k = \frac{2\pi f}{c_2}$. The boundary conditions are

$$\begin{cases} \nabla \bar{T}(\mathbf{r}) \cdot \mathbf{n}_1 = -\frac{ikj_0}{\rho c_p c_2} & \text{for } \mathbf{r} \in \Sigma_1 \\ \nabla \bar{T}(\mathbf{r}) \cdot \mathbf{n}_2 = 0 & \text{for } \mathbf{r} \in \Sigma_2 \end{cases}, \quad (11)$$

where Σ_1 is the heater plate and Σ_2 the thermometer plate. The notations are given in Fig. 15. We propose the method described below, based on the Huygens-Fresnel principle. The principle states that every point

of the wave emitter can be considered as a point source. The linearity of the wave equation can then be used to reconstruct the entire wave by summation of all point source contributions. The Huygens–Fresnel principle has been widely used in the context of electromagnetism, for example to compute diffraction patterns produced by small apertures, or interference patterns... The major difficulty in the context of second sound tweezers is that none of the standard approximations of electromagnetism can be done, neither the far-field approximation nor the small wavelength approximation. This explains why numerical resolution is very useful in this context.

We neglect the tweezers arms, which means that both plates are considered as freestanding, infinitely thin and perfectly insulating plates. We allow a relative inclination γ around the x -axis and a possible relative lateral shift X_{sh} of one plate with respect to the other along the x -axis. We assume that the thermometer is sensitive to the temperature averaged over Σ_2 .

Let us introduce the Green function

$$G(\mathbf{r}) = \frac{1}{|\mathbf{r}|} e^{-ik|\mathbf{r}|}, \quad (12)$$

which is the fundamental solution of the wave equation

$$\Delta G + k^2 G = 4\pi\delta(\mathbf{r}). \quad (13)$$

Let Σ be one of our two square plates, and $U(\mathbf{r}')$ be a smooth function defined over Σ . We introduce the wave defined by

$$\bar{T}(\mathbf{r}) = \frac{-1}{2\pi} \iint_{\Sigma} G(\mathbf{r} - \mathbf{r}') U(\mathbf{r}') d^2\mathbf{r}'. \quad (14)$$

By linearity, \bar{T} is a solution of Eq. (3), for all $\mathbf{r} \notin \Sigma$, because G is a solution. A asymptotic calculation in the vicinity of Σ then shows that \bar{T} satisfies the boundary condition

$$\nabla\bar{T}(\mathbf{r}) \cdot \mathbf{n} \xrightarrow{\mathbf{r} \rightarrow \mathbf{r}_0 \in \Sigma} U(\mathbf{r}_0), \quad (15)$$

where \mathbf{n} is the unit vector normal to Σ and directed inward the cavity (see Fig. 15). We are going to use Eqs. (14) and (15) as the two fundamental relations to build our algorithm. We will compute the solution of the wave equation as an infinite summation of all the emitted and reflected waves in the cavity.

The first wave \bar{T}_1 is emitted by the heating plate Σ_1 and satisfies the first relation in Eq. (11)

$$\nabla\bar{T}_1(\mathbf{r}) \cdot \mathbf{n}_1 = -\frac{ikj_0}{\rho c_p c_2} \quad \text{for } \mathbf{r} \in \Sigma_1.$$

Given Eq. (14) and (15), it is clear that the first wave is given by

$$\bar{T}_1(\mathbf{r}) = \frac{ikj_0}{2\pi\rho c_p c_2} \iint_{\Sigma_1} G(\mathbf{r} - \mathbf{r}') d^2\mathbf{r}_1. \quad (16)$$

Then each time a wave denoted \bar{T}_n hits a plate Σ (Σ_1 or Σ_2), it produces a reflected wave \bar{T}_{n+1} to satisfy the boundary condition

$$\nabla(\bar{T}_n(\mathbf{r}) + \bar{T}_{n+1}(\mathbf{r})) \cdot \mathbf{n} = 0. \quad (17)$$

The situation is sketched in the left panel of Fig. (15). If we choose for \bar{T}_{n+1} the expression

$$\bar{T}_{n+1}(\mathbf{r}) = \frac{1}{2\pi} \iint_{\Sigma} G(\mathbf{r} - \mathbf{r}') [\nabla\bar{T}_n(\mathbf{r}') \cdot \mathbf{n}] d^2\mathbf{r}', \quad (18)$$

then Eq. (15) shows that \bar{T}_{n+1} satisfies the boundary condition

$$\nabla\bar{T}_{n+1}(\mathbf{r}) \cdot \mathbf{n} \xrightarrow{\mathbf{r} \rightarrow \mathbf{r}_0 \in \Sigma} -\nabla\bar{T}_n(\mathbf{r}_0) \cdot \mathbf{n},$$

which is exactly Eq. (17). Eqs. (16) and (18) define our recursive algorithm. Eq. (18) shows that the reflected wave is generated by the gradient of the incident wave. Practically, the recursive computation of all forth and back reflected waves thus requires at each step n the computation of $\nabla\bar{T}_n$ only on the plates, rather than \bar{T}_n . For a reflection at (say) Σ_1 , we have

$$\nabla\bar{T}_{n+1}(\mathbf{r}) \cdot \mathbf{n}_2 = \frac{-1}{2\pi} \iint_{\Sigma_1} G(\mathbf{r} - \mathbf{r}_1) \left[\frac{1}{|\mathbf{r} - \mathbf{r}_1|} + ik \right] \mathbf{n}_2 \cdot \frac{\mathbf{r} - \mathbf{r}_1}{|\mathbf{r} - \mathbf{r}_1|} [\nabla\bar{T}_n(\mathbf{r}_1) \cdot \mathbf{n}_1] d^2\mathbf{r}_1, \quad (19)$$

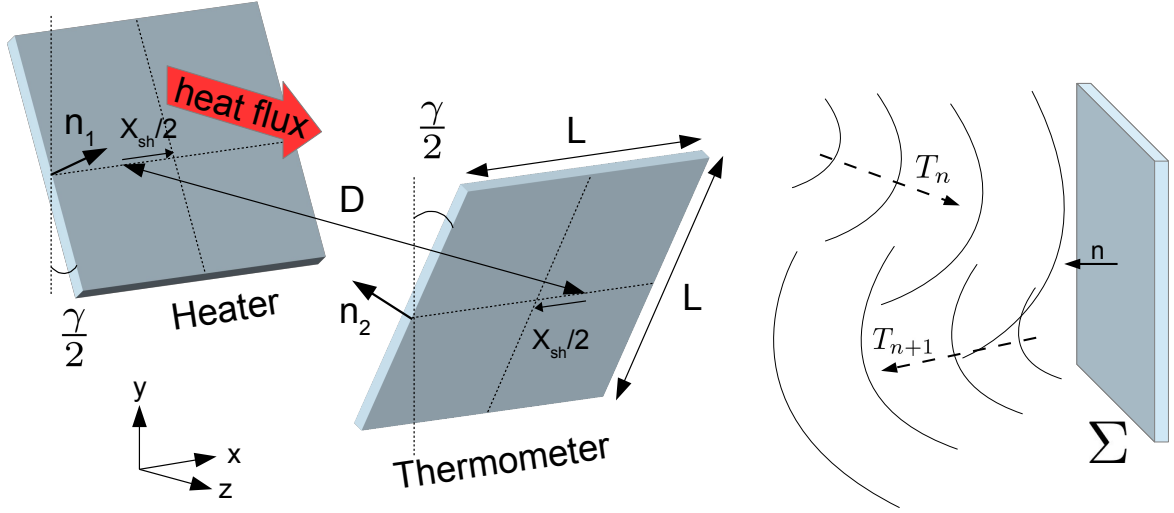


Figure 15: **Left:** Geometrical setup of the numerical algorithm and notations. **Right:** Representation of an incoming and outgoing wave at the n^{th} reflection.

The solution of the wave equation is finally given by the superposition of all waves \bar{T}_n , that is

$$\begin{aligned}\bar{T}(\mathbf{r}) &= \sum_{n=1}^{+\infty} \bar{T}_n(\mathbf{r}), \\ &= \frac{1}{2\pi} \iint_{\Sigma_1} G(\mathbf{r} - \mathbf{r}_1) \sum_{n=0}^{+\infty} [\nabla \bar{T}_{2n+1}(\mathbf{r}_1) \cdot \mathbf{n}_1] d^2\mathbf{r}_1 \\ &\quad + \frac{1}{2\pi} \iint_{\Sigma_2} G(\mathbf{r} - \mathbf{r}_2) \sum_{n=1}^{+\infty} [\nabla \bar{T}_{2n}(\mathbf{r}_2) \cdot \mathbf{n}_2] d^2\mathbf{r}_2.\end{aligned}$$

and the thermometer response is given by

$$\langle \bar{T} \rangle_{\Sigma_2} = \frac{1}{L^2} \iint_{\Sigma_2} \bar{T}(\mathbf{r}) d^2\mathbf{r}.$$

A simulation of the temperature field at $t = 0$ of the 5^{th} resonant mode of second sound tweezers with aspect ratio $\frac{L}{D} = 0.4$, without lateral shift nor inclination of the plates, is displayed in Fig. 16. It can be clearly seen in particular that the amplitude of the temperature field decreases along the z -axis contrary to a Fabry-Perot resonator. This symmetry breaking is due to the diffraction effects associated with the finite size of the plates.

A bulk dissipation can be included in the algorithm, for example, to account for quantum vortex lines inside the cavity. In that case, let ξ be the second-sound attenuation coefficient (in m^{-1}), the wave number $k = \frac{2\pi f}{c_2}$ of the Green function (12) should be replaced by

$$k = \frac{2\pi f}{c_2} - i\xi. \quad (20)$$

3.3.2 In the presence of a turbulent flow

One of the aims of second-sound resonator modelling is to understand their response in the presence of a flow \mathbf{U} sweeping the cavity. One effect of the flow is to advect the second sound wave. In the present section, we explain how the algorithm of sec. 3.3.1 should be modified to account for this effect. We assume in the following that the inequality $|\mathbf{U}| < c_2$ is strictly satisfied, which means that the flow is not supersonic for second sound waves.

In the presence of a non-zero flow \mathbf{U} , the Green function (12) becomes

$$G(\mathbf{r}, t) = \frac{e^{-2i\pi f t^*}}{|\mathbf{r} - \mathbf{U}t^*| \left(1 + \frac{\mathbf{U}}{c_2} \cdot \frac{\mathbf{r} - \mathbf{U}t^*}{|\mathbf{r} - \mathbf{U}t^*|}\right)}, \quad (21)$$

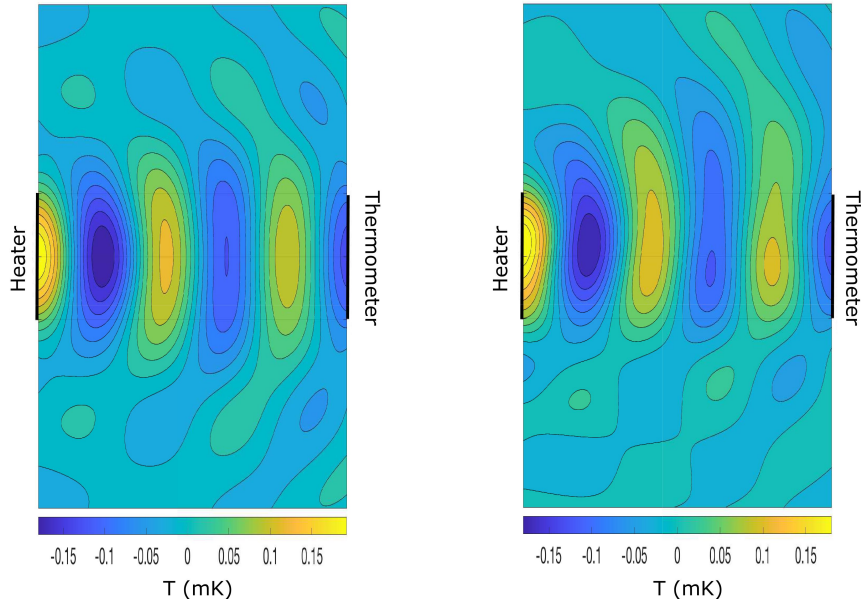


Figure 16: **Left:** Temperature field fluctuations of the 5th resonant mode of second sound tweezers with aspect ratio $\frac{L}{D} = 0.4$, and heating power $j_Q = 0.185 \text{ W/cm}^2$, at the bath temperature $T_0 = 2\text{K}$. **Right:** Temperature field fluctuations for the same conditions with an additional flow of velocity $\frac{U}{c_2} = 0.18$ directed upward. The nodes of the temperature standing wave correspond to antinodes of sound speed velocity, and vice-versa.

where t^* is the time shift corresponding to the signal propagation from the source

$$|\mathbf{r} - \mathbf{U}t^*| = c_2 t^*. \quad (22)$$

In practice, the flow velocity range reached in quantum turbulence experiments is most often much lower than the second sound velocity, with $|\mathbf{U}|$ hardly reaching a few m/s. Most experiments are done in the temperature range where $10 < c_2 < 20 \text{ m/s}$. We thus introduce the small parameter $\beta = \frac{|\mathbf{U}|}{c_2} \ll 1$. Similarly to the standard approximations of electromagnetism, we assume that the effect of β is mostly concentrated in the phase shift $e^{-2i\pi f t^*}$ of Eq. (21). We use the approximation $|\mathbf{r} - \mathbf{U}t^*| \left(1 + \frac{\mathbf{U} \cdot \mathbf{r}}{c_2 |\mathbf{r} - \mathbf{U}t^*|}\right) \approx |\mathbf{r}|$, and we solve Eq. (22) to obtain t^* to leading order in β . The Green function then becomes

$$G(\mathbf{r}, t) = \frac{e^{-ik|\mathbf{r}|\Gamma(\mathbf{r}, \mathbf{U})}}{|\mathbf{r}|}, \quad (23)$$

where as previously $k = \frac{2\pi f}{c_2}$ and

$$\Gamma(\mathbf{r}, \mathbf{U}) = 1 - \frac{\mathbf{U} \cdot \mathbf{r}}{c_2 |\mathbf{r}|}.$$

The algorithm detailed in sec. 3.3.1 can be applied straightforward with the Green function Eq. (23). In particular, Eq. (19) becomes

$$\nabla \bar{T}_{n+1}(\mathbf{r}) \cdot \mathbf{n}_2 = \frac{-1}{2\pi} \iint_{\Sigma_1} G(\mathbf{r} - \mathbf{r}_1, \mathbf{U}) \left[\left(\frac{1}{|\mathbf{r} - \mathbf{r}_1|} + ik \right) \frac{\mathbf{r} - \mathbf{r}_1}{|\mathbf{r} - \mathbf{r}_1|} \cdot \mathbf{n}_2 - ik \frac{\mathbf{U} \cdot \mathbf{n}_2}{c_2} \right] [\nabla \bar{T}_n \cdot \mathbf{n}_1](\mathbf{r}_1) d^2 \mathbf{r}_1. \quad (24)$$

A simulation of the temperature field at $t = 0$ of the 5th resonant mode of second sound tweezers with aspect ratio $\frac{L}{D} = 0.4$, without lateral shift nor inclination, and with a flow of velocity $\frac{U}{c_2} = 0.18$, is displayed in the right panel of Fig. 16. The effect of the flow can be clearly seen with the upward distortion of the antinodes of the wave, compared to the reference temperature profile without flow displayed in the left panel.

3.4 Quantitative predictions

We present in this section the quantitative results obtained with the algorithm of sec. 3.3. The algorithm is specifically run in the configuration of second sound tweezers, but most predictions are relevant for other types

of second sound resonators. We first show that the algorithm can quantitatively account for the experimental spectra. We then use it to predict the response in the presence of a flow and a bulk dissipation in the cavity. The predictions are systematically compared to experimental results for second sound tweezers. We eventually display some experimental observations that illustrate the limits of our model.

3.4.1 Spectral response of second sound resonators

Given a resonator lateral size L , the model of sec. 3.3 has three geometrical parameters : the gap D , the inclination γ and the lateral shift X_{sh} (see notations in Fig. 15). We first sketch qualitatively the importance of those three parameters.

The gap D is the main parameter: it sets the location of the resonant frequencies, and the quality factor of the resonances at low mode numbers. For second sound tweezers, the value of D can be usually obtained within a precision of a few micrometers (D is of the order of 1 millimeter). The relative inclination of the plates γ is responsible for the saturation of the resonant magnitude and its decrease at large mode numbers. It is typically smaller than a few degrees. Contrary to the gap, only the order of magnitude of γ , not its precise value, can be determined from the tweezers spectrum. The lateral shift X_{sh} has very little impact on the spectrum if the value $\frac{X_{sh}}{L}$ remains small enough (we can typically reach $\frac{X_{sh}}{L} < 0.1$ in the tweezers fabrication). However, the effect of this parameter is of paramount importance to understand open cavity resonators response in a flow (such as second sound tweezers), and will be investigated in sec. 3.4.2. We consider the case $X_{sh} = 0$ in the present section. The tweezers size L is known from the probe fabrication process.

The method goes as follows: we first find a gap rough estimation \tilde{D} , for example from the average spacing between the experimental resonant peaks. Then we can run a simulation for parallel plates ($\gamma = 0$), unit gap $D = 1$, and aspect ratio $\frac{L}{\tilde{D}}$, in the range $0 < k^* < n\pi$ (where n is the number of modes to be fitted, and $k^* = kD$ is the non-dimensional wave number). This gives a function $f_{L/\tilde{D}}(k^*)$. The experimental spectrum can then be fitted with the function $T(f) = Af_{L/\tilde{D}}(\frac{2\pi f D}{c_2})$, where A and D are the two free parameters to be fitted, provided the experimental value of c_2 is known. The high sensitivity of the location of the resonant frequencies makes this method very accurate to obtain the gap D .

Once D has been found, new simulations have to be run to find the order of magnitude of γ . As was previously said, γ controls the saturation and the decrease of the resonant magnitudes for large mode numbers. Its value can thus be approximated from a fit of the resonant modes with the largest magnitude. A fit of an experimental tweezers spectrum is displayed in Fig. 17. The values of the fitting parameters for this spectrum are $D = 1.435 \pm 0.003$ mm and $\gamma = 4.2 \pm 0.5$ deg. Given the simplicity of the model assumptions, in particular the assumptions of perfectly insulating and infinitely thin plates without support arms, the agreement with experimental results is very good.

Interestingly, the resonators can also be used in some conditions as thermometers. Once the gap D is known with high enough precision, the spectrum can be fitted using c_2 as a fitting parameter instead of D . Away from the second sound plateau of the curve $c_2(T_0)$ located around 1.65 K, the value of c_2 obtained from the spectrum gives access to the average temperature with a typical accuracy of one mK, simply by inverting the function $c_2(T_0)$.

3.4.2 Response with a flow

Once the characteristics of the resonator have been determined with a background medium at rest, their response in a flow can be studied using the modified algorithm presented in sec. 3.3.2. We experimentally observe that the tweezers response is attenuated in the presence of a superfluid helium flow. This attenuation is related to two physical mechanisms, illustrated in Fig. 18: first, the thermal wave crossing the cavity is damped by the quantum vortices carried by the flow. This type of damping is usually considered as being proportional to the density of quantum vortex lines between the plates. Second, the flow mean velocity is responsible for a ballistic advection of the thermal wave outside the cavity. The thermal wave emitted by the heater partly ‘‘misses’’ the thermometer plate, and, even if the wave is not attenuated, a decrease of the tweezers’ response will be observed. Both mechanisms described above exist in experimental superfluid flows, and cannot be observed independently: once there is a superfluid flow, quantum vortices are created. One key objective is to be able to separate the attenuation of the experimental signal due to bulk attenuation inside the cavity, from the attenuation due to ballistic advection of the wave outside the cavity. We will introduce a mathematical procedure to perform such a separation on a fluctuating signal.

What cannot be experimentally achieved can be simulated with the tweezers model developed in sec. 3.3. The bulk dissipation can be implemented in the algorithm with a wave number complex part ξ (see Eq. (20)), and the flow ballistic deflection can be implemented with a non-zero velocity \mathbf{U} (see Eqs. (23-24)). Both effects can be independently studied, setting alternatively ξ or \mathbf{U} to zero. We first detail below the respective effects

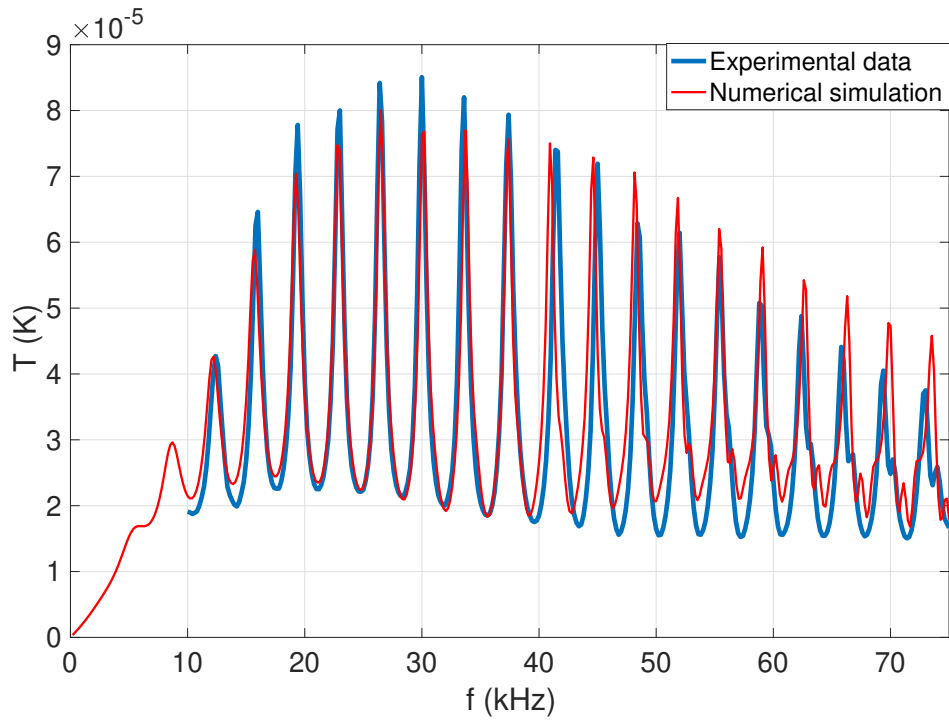


Figure 17: Prediction of the second sound tweezers experimental spectrum of Fig. 11 using the numerical algorithm. The fitting parameters are the gap D , the inclination γ and the total heating power.

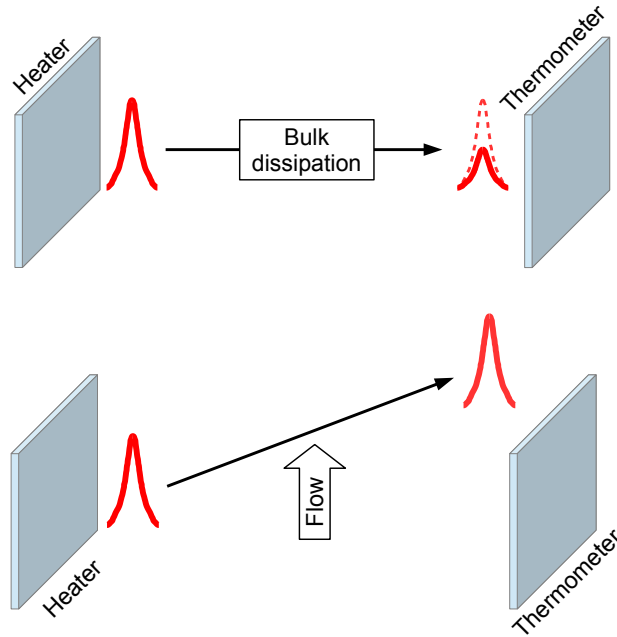


Figure 18: Schematic representation of the two attenuation mechanisms. The top panel illustrates a bulk dissipation of the wave, due for example to the presence of quantum vortices. The bottom panel illustrates the ballistic deflection of the wave by a flow directed parallel to the plates.

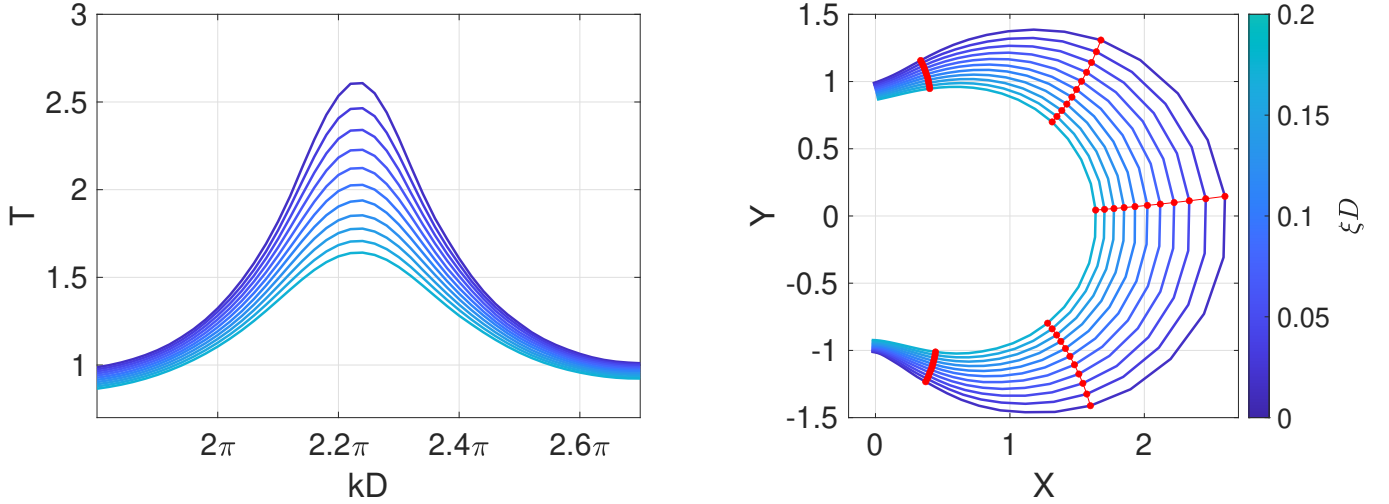


Figure 19: **Numerical simulation:** collapse of a resonance due to increasing values of the bulk attenuation ξ . The left panel display the magnitude of the thermal wave as a function of the wavevector k , and the right panel display the same resonance in the phase-quadrature plane. It can be seen that the bulk attenuation results in an homothetic collapse of the resonance, that means, without global phase shift. For a given value of k , the model predicts that attenuation is directed toward the center of the resonant Kennelly circle (red curves of right panel).

of ξ and \mathbf{U} for perfectly aligned plates ($X_{sh} = 0$).

Fig. 19 display the result of a numerical simulation for second sound tweezers of aspect ratio $L/D = 1$, $\gamma = 0$ and increasing values of bulk dissipation in the range $0 < \xi D < 0.2$. The left panel display the magnitude of the second resonant mode as a function of the wave number, and the right panel display the same resonant mode in the phase-quadrature plane. More precisely, if we call $T(k)$ the thermal wave magnitude recorded by the thermometer, and $\varphi(k)$ its phase, the right panel display the curve $Y(k) = T(k) \sin(\varphi(k))$, $X(k) = T(k) \cos(\varphi(k))$. The resonant curve $(Y(k), X(k))$ is called in the following the resonant “Kennelly circle”, because the curve is very close to a circle crossing the origin. It can even be shown that the resonant curve becomes closer to a perfect circle for increasing resonant quality factors. The major characteristic to be observed in Fig. 19 is that the collapse of the resonant Kennelly circle due to bulk attenuation is homothetic. It means that the different curves have no relative phase shift between each other, when the bulk attenuation increases. The red curves in the right panel display the displacement in the phase-quadrature plane for a fixed value of the wavevector. The model predicts that the displacement is directed toward the Kennelly circle center, which implies that the path at fixed wavevector approximately follows a straight line. By comparison, the left panel of Fig. 21 display an experimental resonance in the phase-quadrature plane, for second sound tweezers of size $L = 1$ mm in superfluid Helium at 1.65 K. The global orientation of the resonant Kennelly circles is simply due to a uniform phase shift introduced by the measurement devices, and should be overlooked. It can be seen that the resonance collapse with increasing values of the flow velocity follows the predictions of Fig. 19: it is homothetic. The red paths correspond to the tweezers signal at fixed heating frequency. Those paths follow approximately a straight line directed to the Kennelly circle center. The slight deviation in the path orientation compared to the predictions of Fig.19 can be explained by a second sound velocity reduction and will be discussed in sec. 3.4.4.

Fig. 20 display the result of a numerical simulation for second sound tweezers of aspect ratio $L/D = 1$, $\gamma = 0$, with $\xi = 0$ and a flow mean velocity $0 < \frac{U}{c_2} < 0.2$. As there is no tweezers lateral shift $X_{sh} = 0$, negative velocities would lead to the same result from symmetry considerations. The figure illustrates the effect of pure ballistic advection on a resonance in the phase-quadrature plane. First, it can be seen that the collapse of the resonant Kennelly circle is accompanied by a relative anti-clockwise phase shift of the curves when the velocity increases. Also, the displacement of the tweezers signal at fixed wavenumber follow the red straight paths directed anti-clockwise. This type of signal strongly contrasts with the one of Fig. 19 obtained for a pure bulk attenuation. The prediction of the left panel in Fig. 20 cannot be directly compared to experiments because, as stated before, a superfluid flow always carries quantum vortices that overwhelm the tweezers signal for tweezers satisfying $X_{sh} \approx 0$.

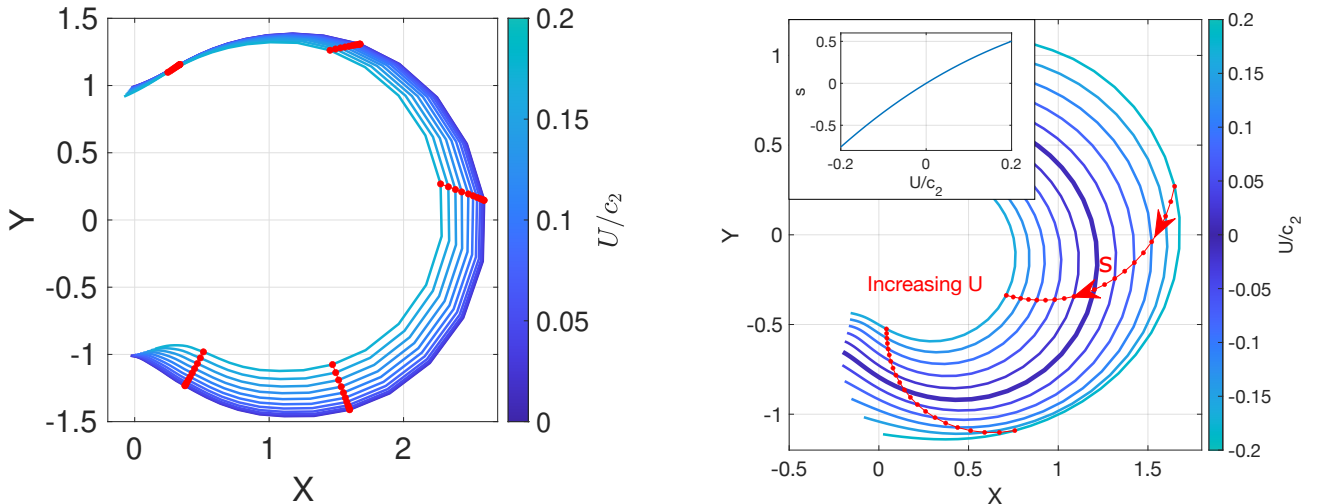


Figure 20: **Numerical simulation:** collapse of a resonance due to ballistic deflection of the thermal wave in the presence of a flow of velocity U , without bulk attenuation ($\xi=0$). The left panel display the result for tweezers without lateral shift ($X_{sh} = 0$). Contrary to the results of Fig. 19, it can be seen in the present case that the collapse is associated with a global anti-clockwise phase shift of the resonant Kennelly circle. Each red curve represents the attenuation at a given value of the wavevector k . The right panel display the result for tweezers with a strong lateral shift $X_{sh} = 0.5 \times L$ (where L is the tweezers size). Such tweezers are very sensitive to the velocity U , with both an attenuation of the resonance and a strong clockwise angular shift of the Kennelly circle. We note s the curvilinear abscissa of the curve obtained at a given value of k (red curve). The inset displays the function $s(U)$. This shows that, once calibrated, second-sound tweezers can be used as anemometers.

3.4.3 Effect of lateral shift of the emitter and receiver plates

We discuss in this section the consequences of a lateral shift, that is $X_{sh} \neq 0$ with the notations of Fig. 15. Contrary to the previous sections, the present discussion is restricted to second sound tweezers, for which a lateral shift has major quantitative effects. A lateral shift would not be as important, for example in the case of wall embedded resonators.

The lateral shift has a marginal effect on the tweezers spectrum when the background fluid is at rest. An effect only appears in the presence of a nonzero velocity specifically oriented in the shifting direction $\mathbf{U} = U\mathbf{e}_x$, because of the mechanism of ballistic advection of the thermal wave by the flow (see the representation of the mechanism in Fig. 18). The importance of this effect depends on the tweezers aspect ratio, on the reduced velocity $\beta = \frac{U}{c_2}$, and on the lateral shift X_{sh} . The lateral shift in the plates' positioning magnifies the signal component related to ballistic advection. This property opens the opportunity to build second sound tweezers for which ballistic advection of the wave completely overwhelms bulk attenuation from the quantum vortices, which means that the tweezers signal is in fact a measure of the velocity component in the shifting direction. We illustrate this mechanism in Fig. 20.

The right panel displays a numerical simulation of a tweezers resonant mode in the phase-quadrature plane, for the parameters $\frac{L}{D} = 1$, $\gamma = 0$ and $X_{sh} = 0.5$, for positive and negative values of the flow velocity in the range $-0.2 < \frac{U}{c_2} < 0.2$. As can be seen at the first sight, the deformation of the resonant curve - that we equivalently call the "Kennelly circle" - is very different from a deformation due to a bulk attenuation (see Fig. 19). First, we observe that the deformation can result in an *increase* of the magnitude of the thermometer signal, when the velocity is negative. This can be explained in this configuration, because the thermal wave emitted by the heating plate is redirected toward the thermometer plate: less energy is scattered outside the cavity when the wave is first emitted by the heater, and the signal magnitude increases. On contrary, the signal magnitude decreases when the velocity is positive because the flow advects the emitted thermal wave further away from the thermometer plate and more energy is scattered outside the cavity. Second, the deformation of the Kennelly circle is associated to a global clockwise rotation, a phenomenon that is not observed for bulk attenuation in Fig. 19. Coming back to Fig. 20, the red curve displays the displacement in the phase-quadrature plane for a fixed wave frequency value. The displacement follows a very characteristic curved path always directed clockwise. Let $s(U)$ be the curvilinear abscissa of the red path. Once calibrated, the value of s can be used as a measure of the flow velocity component in the \mathbf{e}_x direction.

The right panel of Fig. 21 displays the experimental signal observed with second sound tweezers of size

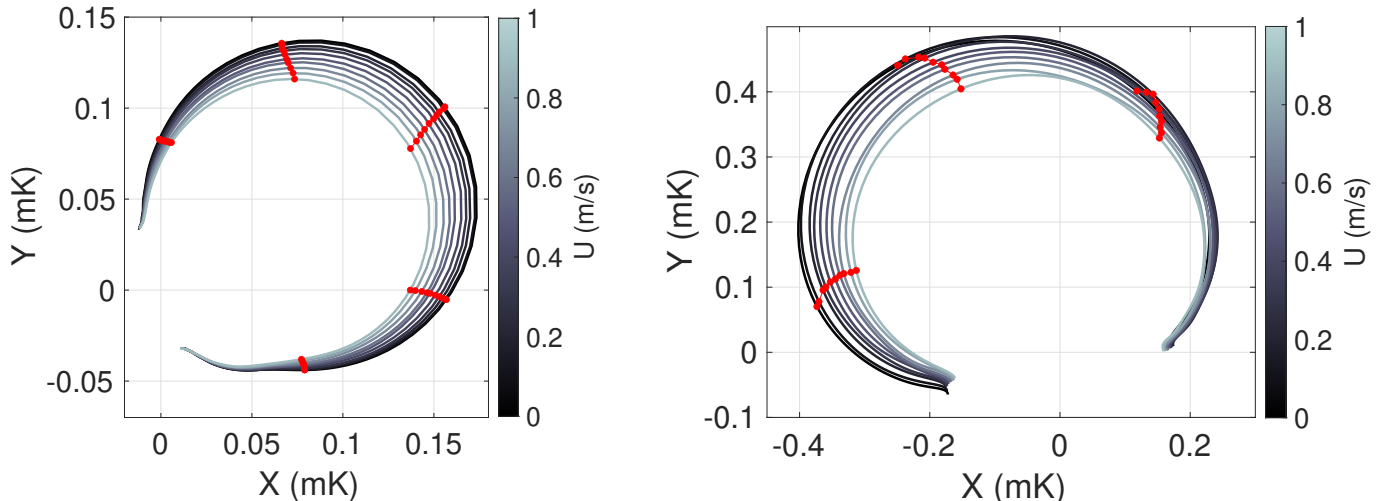


Figure 21: **Experiment:** Collapse of a second sound resonance for increasing values of the flow mean velocity U , in superfluid Helium at $T_0 \approx 1.65$ K. The right panel display the result for tweezers of size $L = 1$ mm and minor lateral shift $X_{sh} < 0.1 \times L$. The figure shows a homothetic collapse of the resonant Kennelly circle without global phase shift, as predicted by the model of Fig. 19. The red curves display the displacement in the phase-quadrature plane at a fixed value of the second sound frequency f . The right panel displays the experimental data obtained with shifted second sound tweezers with parameters $L = 250 \mu\text{m}$ and $X_{sh} = 0.5 \times L$. The figure qualitatively confirms the clockwise angular shift with increasing values of U , predicted by the numerical simulations of Fig. 20.

$L = 250 \mu\text{m}$, $D = 431 \mu\text{m}$ and $X_{sh} \approx 125 \mu\text{m}$, for a positive velocity range $0 < U < 1$ m/s. The main characteristics of a ballistic advection signal can be observed: the Kennelly circle are attenuated with a clear clockwise rotation, and the signal at fixed frequency follows a curved path in the clockwise direction. This is a strong indication that those type of tweezers can be used as anemometers. The signal fluctuations of those type of tweezers were recently characterized in a turbulent flow of superfluid helium [WVR21]. It has been shown in particular that both the signal spectra and its probability distributions indeed display all the characteristics of that of turbulent velocity fluctuations.

3.4.4 Limits of the model

Although the model of sec. 3.3 gives excellent experimental predictions, we still observe some unexpected phenomena with real second sound tweezers. We discuss two of them in this section.

We have seen in secs. 3.4.2 that the thermal wave complex amplitude $\bar{T}(f)$ can be represented in the phase-quadrature plane by a curve $(X(f), Y(f))$ very close to a circle crossing the origin. This osculating circle will be called in the following the resonant “Kennelly circle”. The wave is damped in the presence of a superfluid flow, which can be seen in the phase-quadrature plane as a homothetic shrink of the Kennelly circle toward the origin. Fig. 22 displays an experimental resonance in the phase-quadrature plane, for $U = 0$ m/s and $U = 0.7$ m/s, together with the fitted Kennelly circles. As can be seen in the figure, the resonant curve at $U = 0$ has periodic oscillations in and out the Kennelly circle. We call this phenomenon the “daisy effect”. The daisy effect progressively disappears for increasing values of U , and cannot be seen any more on the resonant curve at $U = 0.7$ m/s. We interpret the daisy effect as a secondary resonance in the experimental setup with a typical acoustic path of a few centimeters. We assume that the flow kicks out the thermal wave from this secondary resonant path when U is increased. The daisy effect alters the attenuation measurements close to $U = 0$, and should be considered with care before assessing the vortex line densities for low mean velocities.

It has been shown in sec. 3.4.2 that the displacement of the tweezers signal in the phase quadrature plane for a fixed wave frequency, follows a straight line. We call “attenuation axis” the direction of this straight path. The model predicts that the attenuation axis should always be directed toward the center of the resonant Kennelly circle. Fig. 23 displays a zoom on a part of the Kennelly circle at $U = 0$, together with the signal displacement at fixed frequency and for increasing flow velocity. It can be seen that the displacement is indeed a straight line, but not exactly directed toward the Kennelly circle center. An angle between 20° and 30° is systematically observed between the attenuation axis and the circle center direction (see Fig. 23). Moreover, the angle is always positive (with the figure convention) and cannot be interpreted as a ballistic advection,

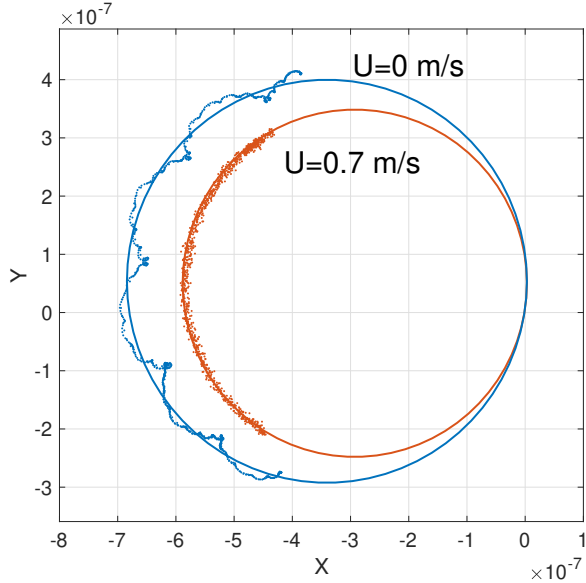


Figure 22: Experimental resonance obtained with a second sound tweezers at 1.98 K, for two values of the He flow mean velocity U . The blue curve displays a periodic perturbation of the resonance that we refer to as the “daisy effect”. The circle is a fit of the Kennelly osculating circle for this resonance. This effect is not predicted by our model, and we interpret it as a secondary resonance in the experimental setup. The daisy effect perturbs the measurements at low values of U , but it can be seen on the red curve that the effect disappears for higher values of U .

that would give a negative angle instead. This effect is thus very likely been attributed to a decrease of the second sound velocity in the presence of the quantum vortices. Whereas a second sound velocity reduction has previously been observed in the presence of quantum vortices [LV74, Meh74, MLM78], the exact value of this reduction turns to be difficult to assess in particular experimental conditions. We therefore keep the second sound velocity reduction as a qualitative explanation, and we do not try to assess quantitative result from the attenuation axis angle.

3.5 Quantum vortex or velocity measurements ?

Let us summarize the discussion of sec 3.4. We have shown that second sound resonators are sensitive to two physical mechanisms. The first one is the thermal wave bulk attenuation inside the tweezers cavity, due to the quantum vortices. The second one is thermal wave ballistic advection perpendicular to the plates⁴. Both mechanisms exist for all the second sound resonators, but depending on their geometry, they can preferentially be sensitive to the one or the other mechanism. We call *selectivity* the fraction of the signal due to quantum vortices or to ballistic advection. Let $\bar{T}(\xi, U)$ be the probe signal as a function of the bulk attenuation coefficient ξ (m^{-1}) and flow velocity U (m/s), we define the vortex selectivity as

$$\mathcal{R}_\xi = \frac{|\bar{T}(\xi, 0) - \bar{T}(0, 0)|}{|\bar{T}(\xi, U) - \bar{T}(0, 0)|}. \quad (25)$$

and by symmetry we define the velocity selectivity as

$$\mathcal{R}_U = \frac{|\bar{T}(0, U) - \bar{T}(0, 0)|}{|\bar{T}(\xi, U) - \bar{T}(0, 0)|}. \quad (26)$$

Further investigations in second sound tweezers experiments have shown that the velocity/vortex selectivity process only weakly depends on the aspect ratio $\frac{L}{D}$. Indeed, for a given resonator lateral size L , ballistic advection of the wave outside the cavity increases when the gap D increases, but the number of quantum vortex lines inside the cavity also increases linearly with D . Altogether, both the ballistic advection and the bulk attenuation due to the quantum vortices have similar dependence with D , that’s why changing the gap has no significant effect on selectivity. For second sound tweezers, we observe that the selectivity neither depends strongly on the mean temperature (that controls the superfluid fraction and the second sound velocity).

⁴Advection of second sound by velocity is illustrated e.g. in [DL77].

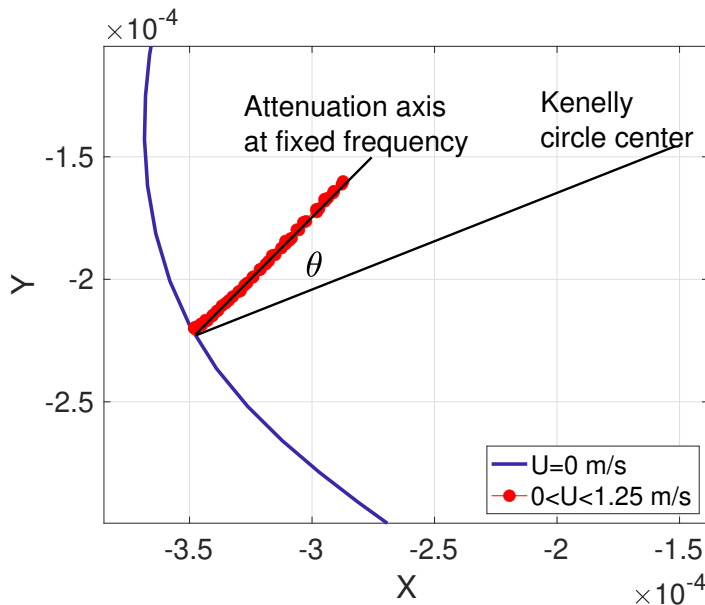


Figure 23: Attenuation of a resonance in the presence of a flow mean velocity U , obtained with second sound tweezers in superfluid Helium at 1.65 K. The blue curve is the resonance at $U = 0$ in the phase-quadrature plane. Contrary to the prediction of the model of section 3.4 (see also Fig. 19), the attenuation signal at fixed heating frequency is not directed exactly toward the centre of the Kennelly osculating circle. We observe a systematic clockwise angular shift $20^\circ < \theta < 30^\circ$. We still have no definite explanation for this observation.

As explained in sec. 3.4.2, the velocity selectivity is more important for open cavity resonators such as second sound tweezers. For a given tweezers size, we find that the selectivity depends mainly on the shift X_{sh} and on the wave mode number. Perfectly aligned tweezers excited with low mode numbers are preferentially sensitive to quantum vortices. Increasing X_{sh} or choosing larger mode numbers leads to a larger velocity sensitivity and changes the signal balance from vortex selectivity to velocity selectivity. The tweezers selectivity also strongly depends on the size L : smaller tweezers can encompass less quantum vortices in the cavity, and are thus less sensitive to quantum vortices, while the velocity sensitivity remains unchanged. The velocity selectivity is thus larger when the tweezers are smaller. Fig. 24 displays the selectivity of two second sound tweezers of size $L = 250 \mu\text{m}$ and $L = 1 \text{ mm}$ respectively, depending on the shift X_{sh} and the mode number n (where $k = n\pi$). The simulation was run with a quantum vortex line density $\mathcal{L} = 2 \times 10^{10} \text{ m}^{-2}$ and $U = 1 \text{ m/s}$, in accordance with the typical values observed in the experiments of [WVR21]. It can be seen that large tweezers ($L = 1 \text{ mm}$) can reach a vortex selectivity $\mathcal{R}_\xi > 90\%$ for a small shift and low mode number, which means that they can be used for direct quantum vortex measurements. On contrary, small tweezers ($L = 250 \mu\text{m}$) can reach a velocity selectivity $\mathcal{R}_U > 90\%$ for large shift or high mode number, and can thus be used as anemometers, as confirmed by the experiments reported in [WVR21].

4 Measurements with second sound tweezers

Second sound tweezers are singular sensors in the sense that they can measure two degrees of freedom at the same time, whereas most of hydrodynamics sensors only measure one (e.g. Pitot tubes, Cantilevers, Hot wires). The tweezers record the magnitude and phase of the thermal wave averaged over the thermometer plate. Both quantities contain physical information about the system. To summarize it shortly, magnitude variations give information about quantum vortices in the cavity, whereas phase variations give information about the local mean temperature and pressure. The local mean velocity has an impact on both magnitude and phase, and will be specifically treated in sec. 4.5. The aim of the following sections is to explain how properly separate quantum vortices signal from other signal components.

In the following, we call \mathcal{L}_\perp the density of projected quantum vortex lines density (projected VLD)

$$\mathcal{L}_\perp = \frac{1}{\mathcal{V}} \int_{\mathcal{V}} \sin^2 \theta(l) dl, \quad (27)$$

where \mathcal{V} is the tweezers cavity volume, l is the curvilinear abscissa along the vortex lines inside the cavity, $\theta(l)$ is the angle between the quantum vortex line and the direction perpendicular to the plates (vector \mathbf{e}_z).

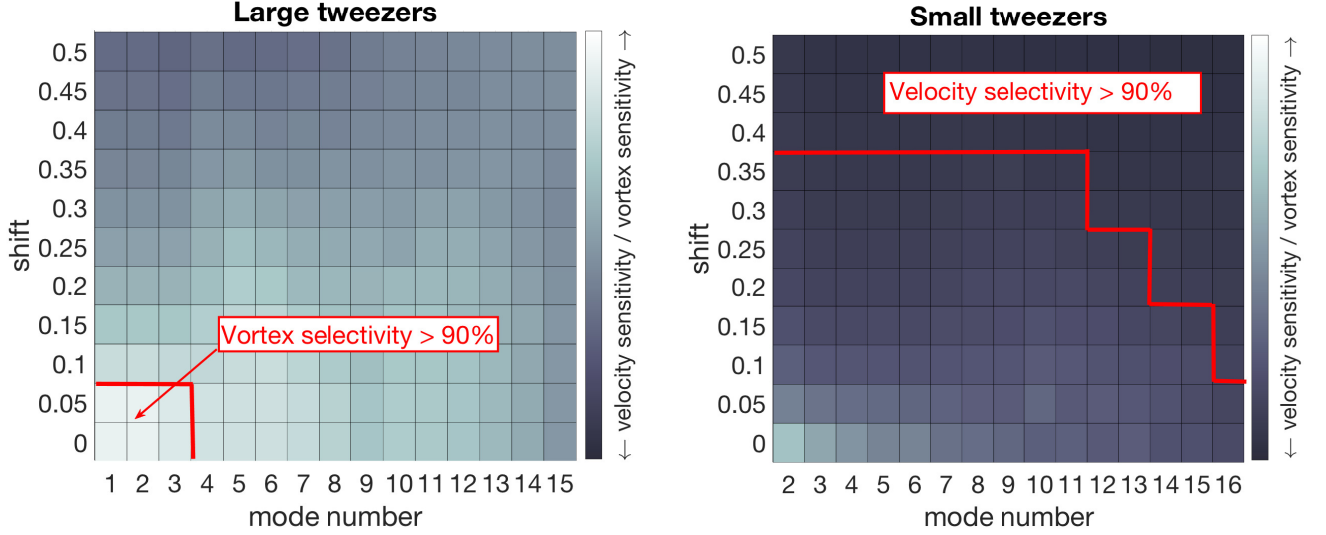


Figure 24: Selectivity to quantum vortices or velocity advection for two second sound tweezers, obtained with numerical simulations. The color code indicates the fraction of the signal due to bulk attenuation by quantum vortices (see Fig. 18). The selectivity of the tweezers mainly depends on the lateral shift of both plates one from another, and the resonant mode number excited in the cavity. The left panel shows that large tweezers ($L = 1\text{mm}$) are mainly sensitive to quantum vortices. Almost pure quantum vortex signal can be achieved with carefully aligned tweezers excited at low mode numbers ($\mathcal{R}_\xi > 90\%$). On the reverse, small tweezers ($L = 250\mu\text{m}$) are mainly sensitive to the velocity. Almost pure velocity signal can be achieved by shifting the heater and the thermometer plates and by exciting the cavity at large mode numbers ($\mathcal{R}_U > 90\%$). The present simulation was run with a vortex line density $\mathcal{L} = 2 \times 10^{10} \text{ m}^{-2}$ and $U = 1 \text{ m/s}$, in accordance with the typical values observed in our experiments.

Assuming isotropy of the vortex tangle, the total quantum vortex lines density (VLD) is

$$\mathcal{L} = \frac{3}{2}\mathcal{L}_\perp. \quad (28)$$

A second sound wave is damped in the presence of a tangle of quantum vortices. Let ξ_{VLD} (in m^{-1}) be the bulk attenuation coefficient of second sound waves, it has been found [HV56a, HV56b, Tsa62, SP66, MPS84] that ξ_{VLD} is proportional to \mathcal{L}_\perp according to the relation

$$\xi_{VLD} = \frac{B\kappa\mathcal{L}_\perp}{4c_2}, \quad (29)$$

where B is the first Vinen coefficient and $\kappa \approx 9.98 \times 10^{-8} \text{ m}^2/\text{s}$ (for ^4He) is the quantum of circulation around one vortex.

Therefore, Eq. (29) shows that a measure of the bulk attenuation coefficient gives access to the projected VLD defined by Eq. (27). We recall in sec. 4.1 the standard methods to measure the bulk attenuation coefficient from a second sound resonance, and we propose in sec. 4.3 a new method called “*the elliptic method*”. We give in sec. 4.4 some examples to apply the elliptic method to the experimental data.

4.1 The vortex line density from the attenuation coefficient

We assume that a single second sound resonance can be accurately represented by the following expression (see Eq. (10))

$$\bar{T}(f) = \bar{T}_0 \frac{\sinh(\xi_0 D)}{\sinh\left(i\frac{2\pi(f-f_0)D}{c_2} + (\xi_0 + \xi_{VLD})D\right)}, \quad (30)$$

where f_0 is the second sound frequency of the local amplitude maximum, D is the resonator gap, c_2 is the second sound velocity, ξ_0 is the attenuation coefficient without flow and ξ_{VLD} is the additional bulk attenuation in the presence of quantum vortices given by Eq. (29). $\xi_{VLD} = 0$ without flow.

A standard method to measure ξ_{VLD} goes as follows: we fix the second sound frequency at the resonant value f_0 , and we measure the thermal wave amplitude with, and without flow. Eq. (30) then shows that ξ_{VLD} is given by

$$\xi_{VLD} = \frac{1}{D} \text{asinh}\left(\frac{\bar{T}_0}{\bar{T}(f_0)} \sinh(\xi_0 D)\right) - \xi_0. \quad (31)$$

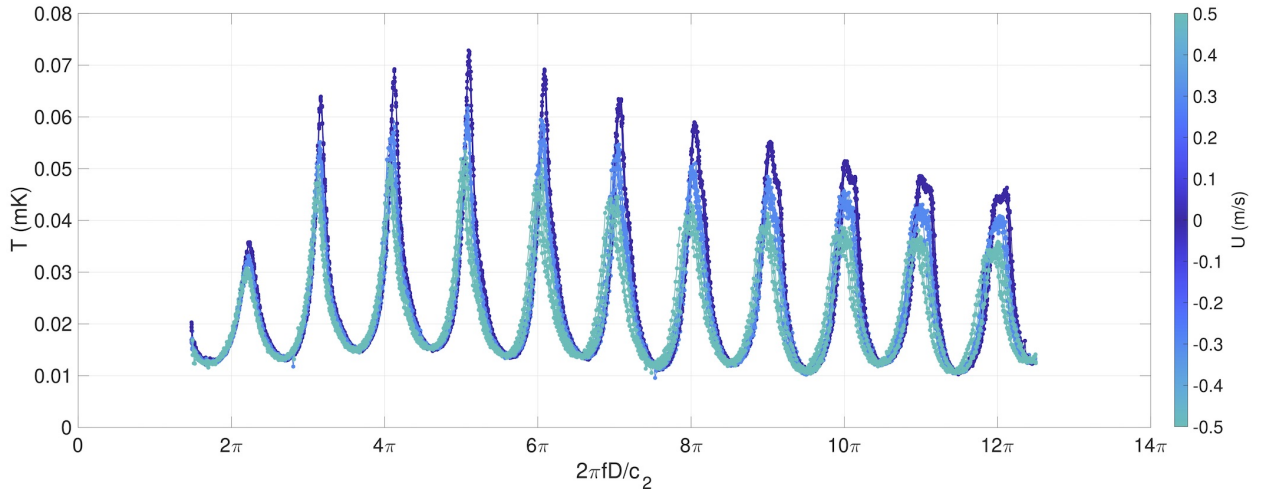


Figure 25: Spectral response of tweezers in the SHREK facility, right below the superfluid transition temperature T_λ , where second sound velocity c_2 is very sensitive to temperature (here $D \simeq 500 \mu\text{m}$ and c_2 drifts around a mean value of 5.4 m/s). The frequency axis is adimensionalize using the second sound velocity c_2 calculated from the temperature recorded near the sidewall of the flow. While the temperature of the bath is regulated, frequency sweeps are repeated half a dozen of times for different turbulent flow conditions flagged by colors. A systematic drift of resonance frequencies versus flow conditions is observed ; it is interpreted as an under-estimation of temperature, and therefore over-estimate of c_2 , due to turbulent dissipation in the core of the flow. At a given mean flow, some scatter of the resonance frequencies is apparent ; it is interpreted as noise from the temperature regulation. The elliptic method introduced in section 4.3 allows separating such temperature artifacts from the attenuation due to second sound attenuation by quantum vortices.

Eq. (31) shows that beside the value of D , that can be determined from a fit of the tweezers spectrum (sec. 3.4), the value of ξ_0 has to be accurately measured. This is usually done by the measurement of the resonant half width. With some algebra manipulations, it can be found from Eq. (30) that the resonant magnitude satisfies

$$|\bar{T}|^2 = |\bar{T}_0|^2 \frac{\sinh^2(\xi_0 D)}{\sinh^2(\xi_0 D) + \sin^2\left(\frac{2\pi(f-f_0)D}{c_2}\right)}. \quad (32)$$

Let Δf be the frequency half-width defined by the relation $|\bar{T}(f_0 \pm \frac{\Delta f}{2})|^2 = \frac{1}{2} |\bar{T}_0|^2$, it can be shown from Eq. (32) that ξ_0 and Δf are related by

$$\sin\left(\frac{\pi \Delta f D}{c_2}\right) = \sinh(\xi_0 D). \quad (33)$$

We note in particular that the relation (33) can be used to find ξ_0 as long as the resonance quality factor is high enough, that means, for $\sinh(\xi_0 D) < 1$. The linear approximations of Eqs. (31) and (33) are usually used when $\xi_0 D \ll 1$, and they give the well-know approximation:

$$\mathcal{L}_\perp \simeq \frac{4\pi \Delta f}{B\kappa} \left(\frac{\bar{T}_0}{\bar{T}(f_0)} - 1 \right), \quad (34)$$

For low quality factor resonances, another method should be used instead of the resonant half width. The elliptic method presented in sec. 4.3 allows determining ξ_0 for resonances of any quality factors.

The main problem of the method presented above is that it implicitly assumes that there is no variation of the acoustic path value $\frac{2\pi f_0 D}{c_2}$ during the measurement. In particular, as c_2 depends on temperature and pressure, it means that the experiment should have an excellent temperature and pressure regulation. This can become increasingly difficult when the second sound derivatives become steep, close to the superfluid transition. Moreover, measurements in the presence of a flow are necessary done out of equilibrium as the flow dissipates energy. As an example, measurements in such conditions are illustrated by figure 25, which shows second sound resonances measured close to the superfluid transition in the turbulent Von Karman experiment SHREK [RBD⁺14]. Furthermore, we observe that a measurement with a non-zero value of ξ_{VLD} can be associated with an acoustic path shift (i.e. a variation of the factor $\frac{2\pi f D}{c_2}$). The situation is illustrated in the left panel of Fig. 26, where the acoustic path shift leads to an overestimation of the attenuation and an important error on ξ_{VLD} .

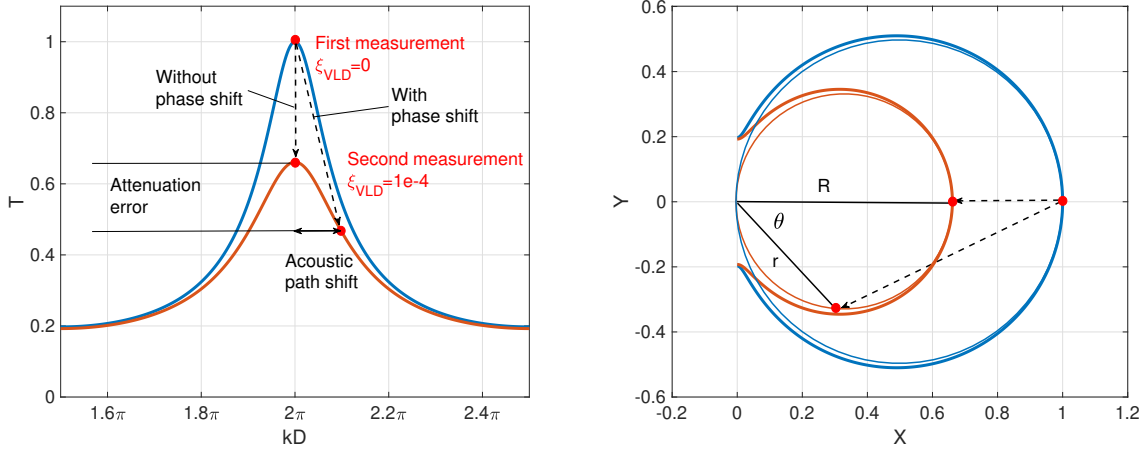


Figure 26: An illustration of an attenuation measurement. **Left:** the resonant mode without (blue curve), and with quantum vortex attenuation (red curve). The figure shows that an acoustic path shift can lead to an important error in the attenuation measurement. **Right:** the resonant mode represented in the phase-quadrature plane together with the fitted Kennelly circle. The figure shows that the acoustic path shift creates a phase shift θ . Using the phase measurement θ , the maximal magnitude can be recovered using Eq. (37).

Passive and active approaches have been reported in the literature to handle the most common cause of acoustical path shift during second sound measurement: the temperature drift and its resulting shift of the resonance frequency.

A passive approach consists in performing a sweep of the second sound frequency, across the resonance curve. Afterward, with proper modelling of the resonance, the attenuation and the phase shift can be fitted separately, e.g. as done in [MSS76]. A limit of this approach is its time resolution, that is restricted by the duration of frequency scan. Another passive approach consists in performing systematic calibration of the full frequency responses of the resonator in various conditions, and subsequently interpolating measurements obtained at a fixed working frequency onto this mapping [VBL⁺17].

A standard example of active approaches consist in controlling the helium bath temperature. An alternative or complementary approach consists in controlling the second-sound frequency so that it always matches the resonance peak, despite possible drift of the temperature. The resonator itself can provide the feedback signal of these control loops, for example by monitoring the thermometer or locking the phase of the second sound signal. An even more direct approach has been recently proposed: the resonator is driven by a self-oscillating circuit, which frequency adapts dynamically to the drift of the second sound velocity [YIE17].

Below, we introduce two analytical methods to separate phase shift from attenuation. The first method is relevant for simple cases (sec. 4.2), while the second one has a broader range of validity (sec. 4.3).

4.2 Analytical method in an idealized case

The acoustic path shift can be corrected using the resonant representation in the phase-quadrature plane. Let $X(f)$ and $Y(f)$ be respectively the real and imaginary parts of $\bar{T}(f)$, the curve $(X(f), Y(f))$ in the phase-quadrature plane is very close to a circle crossing the origin. It can even be proved (see sec. 4.3) that the resonant curve converges to a circle when the quality factor increases, or equivalently when ξ_0 decreases⁵. All along the present article, this limit circle is called the “Kennelly circle”. An illustration of two resonant curves with their osculating Kennelly circles is displayed in the right panel of Fig. 26. The acoustic path shift translates in a phase shift θ in the phase-quadrature plane, such that the amplitude of the second measurement (with $\xi_{VLD} > 0$) does not correspond to the maximal amplitude R of the attenuated resonant peak (see Fig. 26 for

⁵In this case, the complex amplitude of the n^{th} temperature resonance is often approximated by the Lorentzian formula [VS71, DLL80]

$$\bar{T}(f) \simeq \frac{\bar{T}_n}{1 + iQ_n \frac{f-f_n}{f_n}} \quad (35)$$

where \bar{T}_n , Q_n and f_n are the amplitude at resonance, the quality factor and resonance frequency of the mode of interest. To highlight that this Lorentzian approximation describes a circle in the complex plane X - Y , it can be written as:

$$\frac{\bar{T}(f)}{\bar{T}_n/2} = 1 + e^{i\phi(f)} \quad (36)$$

where $\tan \phi = 2F/(F^2 - 1)$ and $F = Q_n(f - f_n)/f_n$.

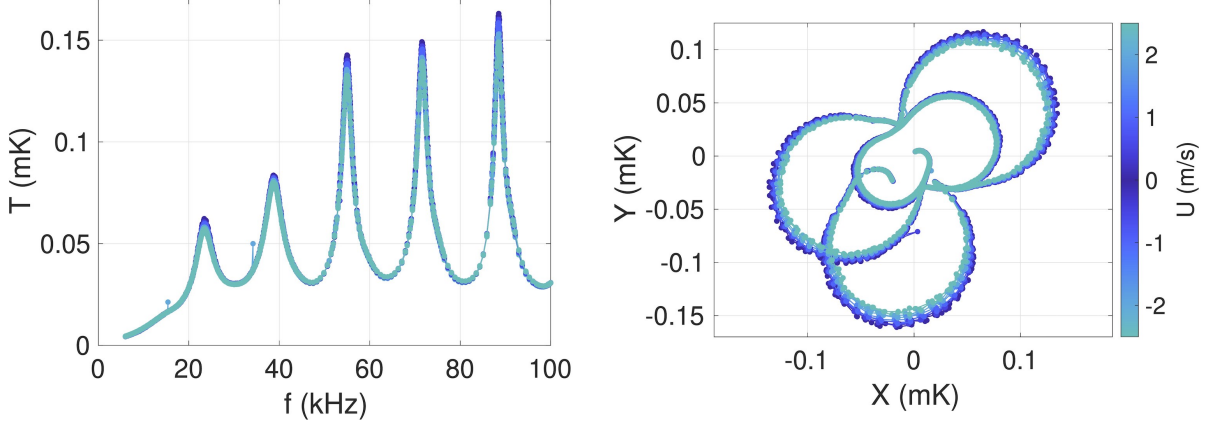


Figure 27: Sequence of five resonances of second sound tweezers at 1.6K. The flow is weakly turbulent: the velocity standard deviation is a few percents of the mean velocity displayed on the colorbar. The right side plot illustrates that each resonance can be approximated by a circle in the complex plane. The global phase shift of the last resonance (lower circle) compared to the others is attributed to a cut-off of the measurement electronics at high frequency.

the notations). Using the geometric properties of the Kennelly circle, R can be approximately recovered from the measured amplitude r with

$$R = \frac{r}{\cos \theta}. \quad (37)$$

Thus, a modified version of Eq. (31) can be written to find the VLD attenuation coefficient in the presence of a phase shift

$$\xi_{VLD} = \frac{1}{D} \operatorname{asinh} \left(\frac{\bar{T}_0 \cos \theta}{\bar{T}(f_0) e^{-i\theta}} \sinh(\xi_0 D) \right) - \xi_0. \quad (38)$$

4.3 The elliptic method

We present in this section an original method to obtain the values of the acoustic path shift and the attenuation coefficient, from experimental data. The method, that we call the “elliptic method”, is much simpler to implement, and much more reliable, than the fit of the Kennelly resonant circle and the use of Eq. (38). Besides, the method can be used for resonances with very low quality factors.

The method comes from the observation that a pair of two ideal consecutive resonances is transformed into an ellipse with the complex inversion $z \rightarrow \frac{1}{z}$ in the phase-quadrature plane. The inversion is represented in Fig. 28. To prove this assertion, consider the inversion of the classical Fabry–Perot expression Eq. (6)

$$\frac{1}{\bar{T}} = \frac{\sinh \left(i \frac{2\pi f D}{c_2} + \xi D \right)}{A}. \quad (39)$$

Expanding the sinh in the previous expression gives

$$\frac{1}{\bar{T}} = \cos \left(\frac{2\pi f D}{c_2} \right) \frac{\sinh(\xi D)}{A} + i \sin \left(\frac{2\pi f D}{c_2} \right) \frac{\cosh(\xi D)}{A}. \quad (40)$$

Finally, let $X_l = \operatorname{Re} \left(\frac{1}{\bar{T}} \right)$ and $Y_l = \operatorname{Im} \left(\frac{1}{\bar{T}} \right)$ be respectively the real and imaginary parts of Eq. (40), the coordinates (X_l, Y_l) satisfy the equation

$$\left(\frac{X_l}{\sinh(\xi D)/A} \right)^2 + \left(\frac{Y_l}{\cosh(\xi D)/A} \right)^2 = 1 \quad (41)$$

which is exactly the cartesian equation of an ellipse with semi-major axis $a = \frac{\cosh(\xi D)}{A}$, and semi-minor axis $b = \frac{\sinh(\xi D)}{A}$. In particular, we note that the attenuation coefficient ξ can be recovered from the ratio of the semi-major and semi-minor elliptic axes using the formula

$$\xi = \frac{1}{D} \operatorname{atanh} \left(\frac{b}{a} \right).$$

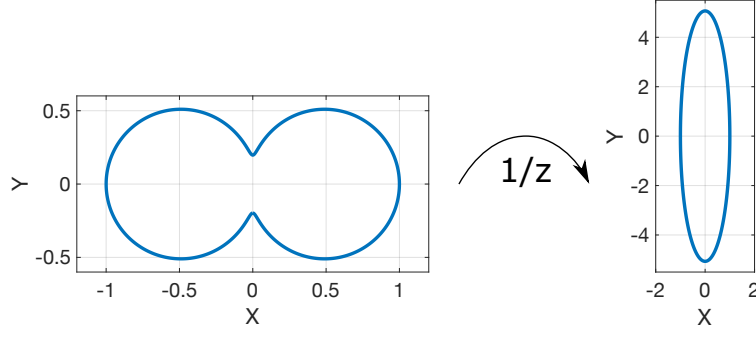


Figure 28: Transformation of a pair of consecutive resonances to an ellipse using the inversion of the complex plane $z \rightarrow 1/z$.

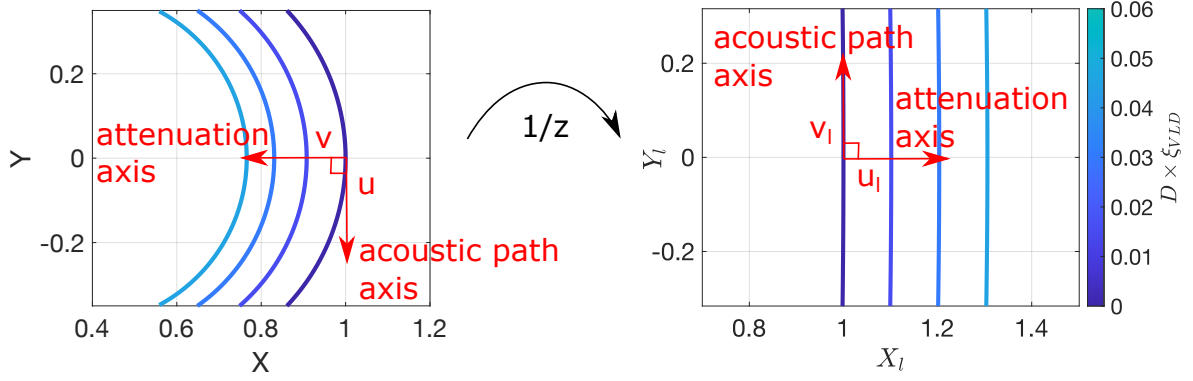


Figure 29: A resonant mode in the phase-quadrature plane and its elliptic transform, for an ideal Fabry–perot resonance with $\xi_0 = 0.2$ and $1.95\pi < kD < 2.05\pi$.

When the quality factor increases (equivalently when ξ decreases) the ellipse is flattened. The limit of infinite quality factor ($\xi \rightarrow 0$) corresponds to two parallel straight lines in the complex plane.

Second sound tweezers resonances are not ideal Fabry–Perot resonances. Yet, we have argued in sec. 3.2 that a single second sound resonance can be locally fitted by the following Fabry–Perot equation (see also Eq. (10))

$$\bar{T} = \frac{A}{\sinh\left(i\frac{2\pi(f-f_0)D}{c_2} + (\xi_0 + \xi_{VLD})D\right)}. \quad (42)$$

This in particular means that the resonant curve in the vicinity of its maximal amplitude is transformed into a part of an ellipse with the complex inversion $z \rightarrow \frac{1}{z}$. The curve $(X_l(f), Y_l(f))$ is very close to a straight line, for frequencies f close to the resonant frequency f_0 . The situation is illustrated in Fig. 29. The figure shows a part of ideal Fabry–Perot resonances given by Eq. (42), in the range $1.95\pi < kD < 2.05\pi$ (where $k = \frac{2\pi f}{c_2}$), and for increasing values of the VLD attenuation coefficient ξ_{VLD} . The left panel displays the different resonant curves close to their maximal amplitudes, in the phase-quadrature plane. Using the complex inversion, those curves become almost parallel straight lines, as can be seen in the right panel. The transformation of the resonant Kennelly circles into parallel straight lines has very nice applications that we explain in the following.

In the phase-quadrature plane, a variation of the acoustic path value $\frac{2\pi f D}{c_2}$ corresponds to a displacement along the Kennelly circle, whereas a variation of the bulk attenuation ξ corresponds to a displacement orthogonal to the Kennelly circle. The acoustic path direction and the attenuation direction thus form a local orthogonal basis. Such a basis is displayed by the red arrows in the left panel of Fig. 29. When the reference point where the basis is defined moves along the Kennelly circle, the basis rotates and the acoustic path and attenuation axes have to be redefined. This can become a tiresome task while analyzing the experimental data. Fortunately, the complex inversion is a conformal mapping, which means that it preserves locally the angles: the local basis composed of the acoustic path and attenuation axes is transformed into an orthogonal basis (see the red arrows in the right panel of Fig. 29). More precisely, let z_0 be the complex position in the phase-quadrature plane,

and (\mathbf{u}, \mathbf{v}) be the two complex (unit) vectors defining the local basis at z_0 , then the local basis $(\mathbf{u}_l, \mathbf{v}_l)$ at the point $\frac{1}{z_0}$ is given by

$$\begin{cases} \mathbf{u}_l &= -\mathbf{u} \frac{|z_0|^2}{z_0^2} \\ \mathbf{v}_l &= -\mathbf{v} \frac{|z_0|^2}{z_0^2} \end{cases} \quad (43)$$

The major advantage of defining the local basis $(\mathbf{u}_l, \mathbf{v}_l)$ with the elliptic transform, is that it becomes a *global* basis: when the reference point $\frac{1}{z_0}$ moves because of a change in the acoustic path value or the attenuation value, the basis is simply translated in the plane but the vectors $(\mathbf{u}_l, \mathbf{v}_l)$ do not change. One can find the global basis (\mathbf{u}, \mathbf{v}) for a given resonance and use it to find the local basis $(\mathbf{u}_l, \mathbf{v}_l)$ at every point in the phase-quadrature plane. We will see in sec. 4.4.1 how the global basis (\mathbf{u}, \mathbf{v}) can be easily used to suppress temperature and pressure drifts during second sound attenuation measurements.

We finally explain how the elliptic method can be used to measure the bulk attenuation coefficient ξ_0 . We have seen in sec. 4.1 that the standard methods to find ξ_0 are based on the measure of the half-width Δf and on Eq. (33). As was said previously, the classical method can only be applied to resonances satisfying $(\xi_0 D) < 1$. It is a global method, in the sense that one has to sweep the frequency to measure a large part of the resonant curve. The method is only accurate provided the resonance does not deviate too much from an ideal Fabry–Perot resonance, which is often not satisfied for the first modes of second sound tweezers (see for example the first mode of Fig. 17). The alternative method consists in expanding (X_l, Y_l) given by Eq. (41) to leading order in $f - f_0$

$$\begin{cases} X_l &\sim \frac{\sinh(\xi_0 D)}{A}, \\ Y_l &\sim \frac{2\pi(f-f_0)D}{c_2} \frac{\cosh(\xi_0 D)}{A}, \end{cases} \quad (44)$$

where f_0 is the resonant frequency. Using Eq. (44), we get

$$\frac{Y_l(f)}{X_l(f)} \sim \frac{2\pi D}{\tanh(\xi_0 D) c_2} (f - f_0). \quad (45)$$

$\frac{Y_l(f)}{X_l(f)}$ is proportional to f in the vicinity of f_0 , with the proportionality factor $\frac{2\pi D}{\tanh(\xi_0 D) c_2}$. The attenuation coefficient ξ_0 can be found by a linear fit of the function $\frac{Y_l}{X_l}$ provided D and c_2 are known.

4.4 Applications of the elliptic method

The motivation to develop and use the elliptic method has come from experimental constrains: in a large superfluid experiment, it can be very difficult to control the values of mean temperature and pressure. This is even more the case if the superfluid experiment dissipates energy. One then expects a drift of the thermodynamics conditions during the measurement. Regarding second sound resonators, the critical parameter is the second sound velocity c_2 , because variations lead to uncontrolled acoustic path shifts. The elliptic method has been designed to easily filter those variations from experimental data. This includes filtering temperature and pressure drifts (sec. 4.4.1) and the vibration of the tweezers arms (sec. 4.4.3), and properly extract the quantum vortex lines fluctuations (sec. 4.4.2).

4.4.1 Suppression of temperature and pressure drifts

This section presents an example of the elliptic method implementation for second sound tweezers, to find the relation between $\langle \xi_{VLD} \rangle$ and the mean velocity U in the presence of a superfluid flow.

As before, we note (X, Y) the temperature signal obtained from the second sound tweezers in the phase-quadrature plane, and (X_l, Y_l) the cartesian coordinates obtained by the complex inversion given by

$$\begin{cases} X_l &= \mathcal{R}e \left(\frac{1}{X+iY} \right), \\ Y_l &= \mathcal{I}m \left(\frac{1}{X+iY} \right). \end{cases} \quad (46)$$

The coordinates (X_l, Y_l) will be called “elliptic coordinates” for convenience. Fig. 30 displays experimental data obtained from second sound tweezers of size $L = 1$ mm, in a saturated bath at mean temperature $T_0 \approx 2.14$ K, and for different mean flow velocities $0 < U < 1.2$ m/s. At such a temperature close to the superfluid transition, it was difficult to regulate the mean temperature and therefore the second sound velocity. Uncontrolled acoustic path variations can be observed, for example in the red points of Fig. 30.

The first step consists in sweeping the second sound frequency f in the vicinity of the resonant frequency f_0 . The data (X, Y) obtained, displayed by the black curve of the left panel of Fig. 30, form a part of the Kennelly circle. As explained in sec. 4.3, the elliptic coordinates (X_l, Y_l) given by Eq. (46) form a straight line (see the

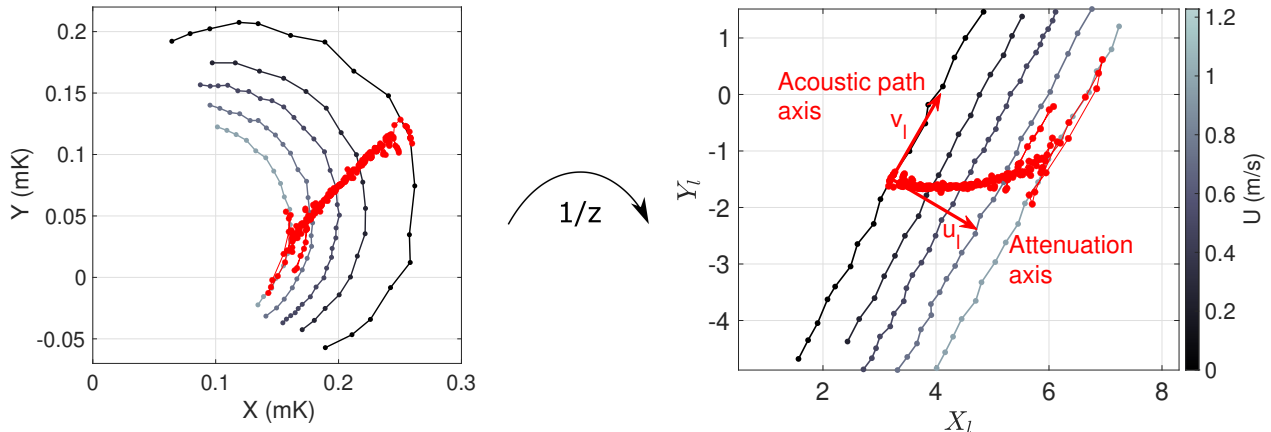


Figure 30: **Experiment:** measurement of a resonance with second sound tweezers at $T_0 \approx 2.14$ K, for different values of the mean flow velocity U . The left panel presents the data in the phase-quadrature plane, and the right panel presents the same data after the complex inversion. The red points are obtained for a fixed value $f = 6.35$ kHz, and sweeping the flow mean velocity between 0 and 1.2 m/s.

right panel of Fig. 30). Using a linear fit, it is then straightforward to obtain the unit vector \mathbf{v}_l parallel to the line defining the acoustic path axis, and the orthogonal vector \mathbf{u}_l defining the attenuation axis. We then call $\mathbf{Z}_l = (X_l, Y_l)$ the vector of the elliptic coordinates. The attenuation coefficient ξ_0 can be found by the relation (see Eq. (45))

$$\frac{\mathbf{Z}_l(f) \cdot \mathbf{v}_l}{\mathbf{Z}_l(f) \cdot \mathbf{u}_l} \sim \frac{2\pi D}{\tanh(\xi_0 D) c_2} (f - f_0).$$

Fig. 30 displays experimental resonant curves obtained for non-zero mean velocities $U > 0$, to illustrate the robustness of the elliptic method. However, we emphasize that only the resonant curve with $U = 0$ is necessary to find the global basis $(\mathbf{u}_l, \mathbf{v}_l)$ in the plane of elliptic coordinates.

The second step consists in fixing the second sound frequency to f_0 and vary the mean velocity U to look at the resonance attenuation. The experimental data are displayed by the red points in Fig. 30. In can be seen in the figure that the bulk attenuation is accompanied by a systematic acoustic path deviation as the mean velocity increases. For mean velocities $U \approx 1$ m/s, energy dissipation in the experiment leads to a data dispersion along the acoustic path direction. To properly recover the mean VLD attenuation coefficient $\langle \xi_{VLD} \rangle$, we use the elliptic coordinates $\mathbf{Z}_l = (X_l, Y_l)$, and we project it on the attenuation axis \mathbf{u}_l . We get from Eq. (44)

$$\frac{\mathbf{Z}_l(U) \cdot \mathbf{u}_l}{\mathbf{Z}_l(0) \cdot \mathbf{u}_l} = \frac{\sinh((\xi_0 + \langle \xi_{VLD} \rangle) D)}{\sinh(\xi_0 D)}.$$

And $\langle \xi_{VLD} \rangle$ is then given by

$$\langle \xi_{VLD} \rangle = \frac{1}{D} \operatorname{asinh} \left(\frac{\mathbf{Z}_l(U) \cdot \mathbf{u}_l}{\mathbf{Z}_l(0) \cdot \mathbf{u}_l} \sinh(\xi_0 D) \right) - \xi_0. \quad (47)$$

We note that the previous expression remains accurate even if the second sound frequency chosen for the measurement is close but not exactly equal to the resonant frequency f_0 . The average VLD attenuation can then be converted to the average projected vortex line density $\langle \mathcal{L}_\perp \rangle$ using Eq. (29).

4.4.2 Measure of vortex line density fluctuations

Second sound tweezers are designed to directly probe the small scale vortex line density fluctuations, not only its average value. The method to probe fluctuations slightly differs from the method used to probe the average value explained in sec. 4.4.1. The average VLD value can be directly computed using the complex inversion of experimental data, but this is no longer possible for its fluctuations. Indeed, the tweezers signal have different sources of noise, like e.g. thermal white noise, interfering frequencies, electromagnetic bursts, etc... Those signals can usually be considered as independent additive noises in the signal data, and easily filtered out or attenuated by an appropriate post-processing. On the contrary, the complex inversion is a non-linear transformation. Using the latter on noisy data can lead to an overestimation of the signal fluctuations closest to zero,

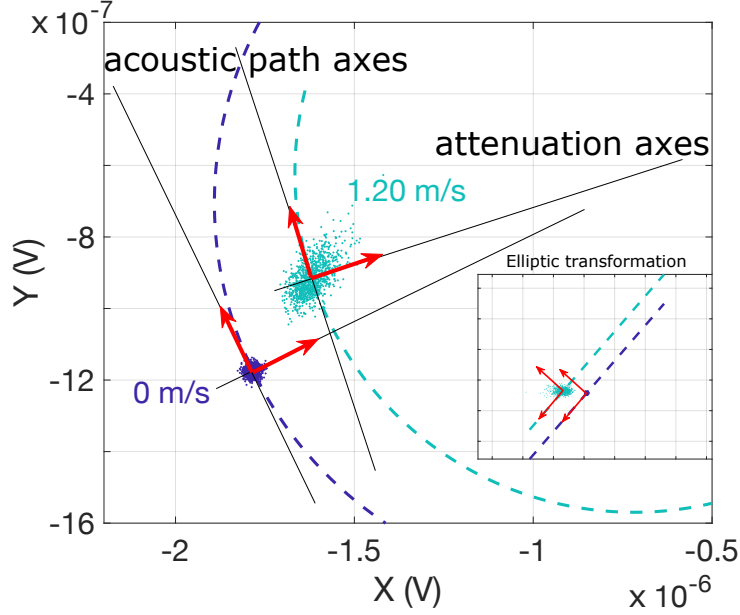


Figure 31:

perturb the additivity of noise sources and make them much more difficult to filter out. We thus choose to compute the VLD fluctuations only using linear transformations.

The first step is similar to that of sec. 4.4.1. We sweep the second sound frequency f close to the resonant frequency f_0 , in order to measure a part of the Kennelly circle. We then transform this Kennelly circle into a straight line using the complex inversion, and we find the global basis $(\mathbf{u}_l, \mathbf{v}_l)$ in the plane of elliptic coordinates. A fit of the Kennelly circle, and its transformation into a straight line can be seen in Fig. 31. This experimental step has to be done just before the fluctuations measurement.

We then record the signal fluctuations $(X(t), Y(t))$, for different values of the flow mean velocity U . Fig. 31 displays the fluctuating signal for $U = 0$ and $U = 1.2$ m/s in the form of clouds of data points. It can be in particular observed that the $U = 1.2$ m/s data are shifted compared to the $U = 0$ m/s data because of both an average attenuation and an acoustic path shift (see sec. 4.4.1). Let us define $\langle \mathbf{Z}(t) \rangle = \langle X(t) + iY(t) \rangle$ the average complex position in the phase-quadrature plane, for a given value of U . Following Eq. (43), the local basis (\mathbf{u}, \mathbf{v}) of the attenuation and acoustic path axes can be computed from the global elliptic basis $(\mathbf{u}_l, \mathbf{v}_l)$ by

$$\begin{cases} \mathbf{u} &= -\mathbf{u}_l \frac{\langle \mathbf{Z} \rangle^2}{|\langle \mathbf{Z} \rangle|^2} \\ \mathbf{v} &= -\mathbf{v}_l \frac{\langle \mathbf{Z} \rangle^2}{|\langle \mathbf{Z} \rangle|^2} \end{cases} \quad (48)$$

Fig. 31 shows that the local basis (\mathbf{u}, \mathbf{v}) depends on $\langle \mathbf{Z} \rangle$ and thus on the value of U : for different mean velocities, the bases are rotated from one another. If there is a significant drift of the mean signal value during the measurement (as can e.g. be observed in Fig. 22), the local basis will also depend on time, with a typical timescale that should be much larger than the fluctuation timescale.

The acoustic path fluctuations and the attenuation fluctuations can then be recovered using a projection on the (\mathbf{u}, \mathbf{v}) basis. More precisely, let x be the average acoustic path value and $\delta\xi = \xi - \langle \xi \rangle$ be a small fluctuation of the attenuation coefficient, a leading order expansion of expression Eq. (42) shows that

$$\bar{T} \approx \frac{A}{\sinh(ix + \langle \xi \rangle D)} - \delta\xi \frac{AD}{\sinh(ix + \langle \xi \rangle D) \tanh(ix + \langle \xi \rangle D)}. \quad (49)$$

We then do the approximation $\langle \mathbf{Z} \rangle \approx A / \sinh(ix + (\xi_0 + \langle \xi_{VLD} \rangle) D)$ which is equivalent to neglecting non-linear corrections in Eq. (49). We finally get

$$\delta\xi(t) = \frac{1}{D} \mathbf{u} \cdot (\mathbf{Z}(t) - \langle \mathbf{Z} \rangle) \times \left| \frac{\tanh(ix + (\xi_0 + \langle \xi_{VLD} \rangle) D)}{\langle \mathbf{Z} \rangle} \right|, \quad (50)$$

where the value of ξ_0 can be found with Eq. (45) and $\langle \xi_{VLD} \rangle$ with Eq. (47).

The use of the elliptic method is illustrated by Figure 32, which reports the probability density function of the fluctuations of the quantum vortex density in a nearly isotropic superfluid turbulent flow. The data of this

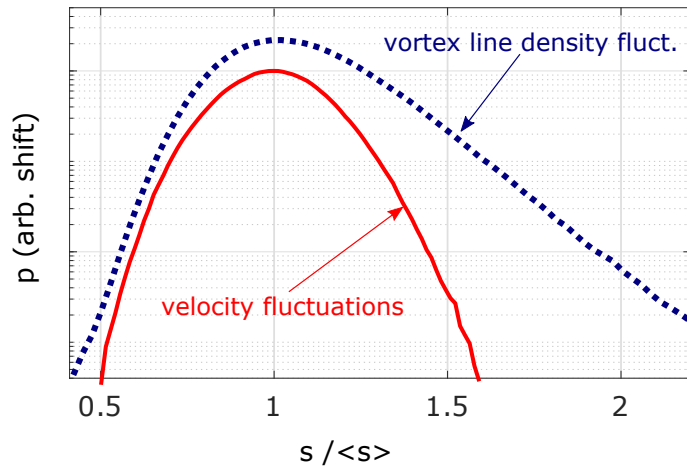


Figure 32: Example of the probability density function of vortex line density (dashed line) and velocity (continuous line) measured by second sound tweezers in a superfluid turbulent flow [WVR21]. In abscissa, each signal s is normalized by its mean value $\langle s \rangle$. The nearly Gaussian velocity statistics and skewed vorticity statistics are reminiscent of those in classical turbulence.

plot were reported together with spectra of vorticity fluctuations. For details about the setup and analysis of these results, see [WVR21].

4.4.3 Filtering the vibration of the plates

One possible source of noise for second sound resonator measurement is the vibration of the plates arms whenever $U \neq 0$. The signature of those vibrations can be very clearly identified in the form of two thin peaks in the fluctuations power spectrum. Those two peaks are located at the two arms resonant frequencies: their exact values can vary for different tweezers, but we always observe them around $f \approx 1$ kHz (see sec. 4.4).

Fortunately, the tweezers arms vibrations correspond to a variation of the gap D , and thus to acoustic path fluctuations. Fig. 33 display a part of the tweezers fluctuations power spectrum. The fluctuations are projected along the attenuation axis (blue curve) and along the acoustic path axis (red curve), following the method presented in sec. 4.4.2. The two peaks located at $f \approx 825$ Hz and $f \approx 1050$ Hz are identified on the acoustic path axis fluctuations power spectrum, whereas the same peaks are damped by many orders of magnitude on the attenuation axis fluctuations. Using the power spectrum of Fig. 33, we can estimate the order of magnitude of the gap standard deviation. We find $\sqrt{\langle (\delta D)^2 \rangle} \approx 0.5 \mu\text{m}$, and $\frac{\sqrt{\langle (\delta D)^2 \rangle}}{D} \approx 4 \times 10^{-4}$. This confirms that the arms vibrations have a negligible impact on the measurement.

4.5 Velocity measurements

As shown in Sec. 3.5, the second sound tweezers geometry can be optimized to sense specifically velocity rather than vortex density. For this purpose, one trick consists in shifting one plate with respect to the other in the flow direction. Figure 34 shows three second sound tweezers and one anemometer that is based on the same principle as Pitot tubes. All sensors are positioned across a nearly isotropic superfluid flow bounded by a cylindrical pipe -not shown here- (for details on this set-up, see [RCSR17a]). The figure insert is a close view of the tip of the left-side tweezers, which is dedicated to velocity measurements. This shift of one plate versus the other in the downstream direction is clearly visible.

The projection of the anemometer-tweezers signal in the complex plane is not performed along orthogonal axes. These axes are determined with an in-situ calibration, ramping the mean velocity. The complementary ‘‘Pitot tube’’ signal is used to calibrate the axis in units of m/s. The duration of velocity ramp is chosen to be much larger than the time resolution of the Pitot tube.

As an illustration, Figure 32 presents the probability density function of the velocity fluctuations measured by the anemometer tweezers, together with vortex line density fluctuations recorded by the other tweezers during the same experimental run (see Fig. 34). As expected in nearly homogeneous and isotropic quantum turbulence [SCLR12], the velocity statistics are close to a Gaussian when probed at scales significantly larger than the intervortex distance, which is the case here. Velocity spectra derived from the same dataset are reported in [WVR21].

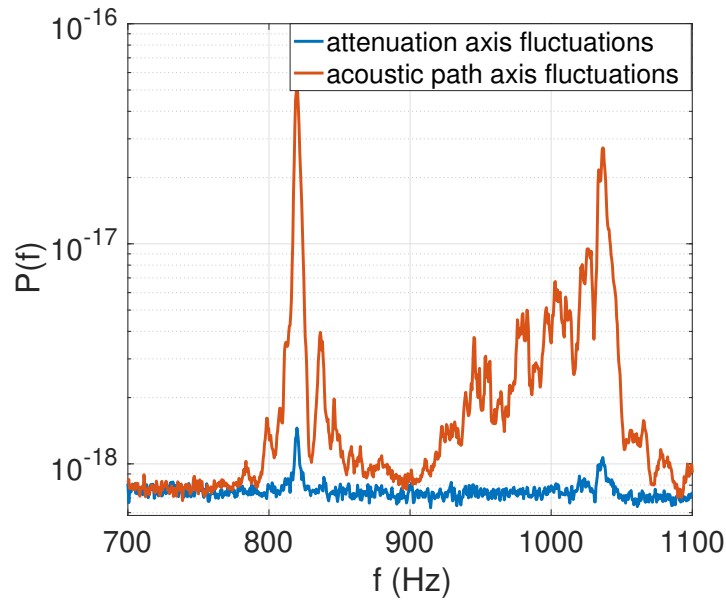


Figure 33: **Experiment:** a part of second sound tweezers fluctuation power spectrum, with $T_0 = 1.65$ K, $U = 1.2$ m/s and for a tweezers gap $D = 1.320$ mm. The tweezers arms' resonances can be clearly identified in the acoustic path fluctuations.

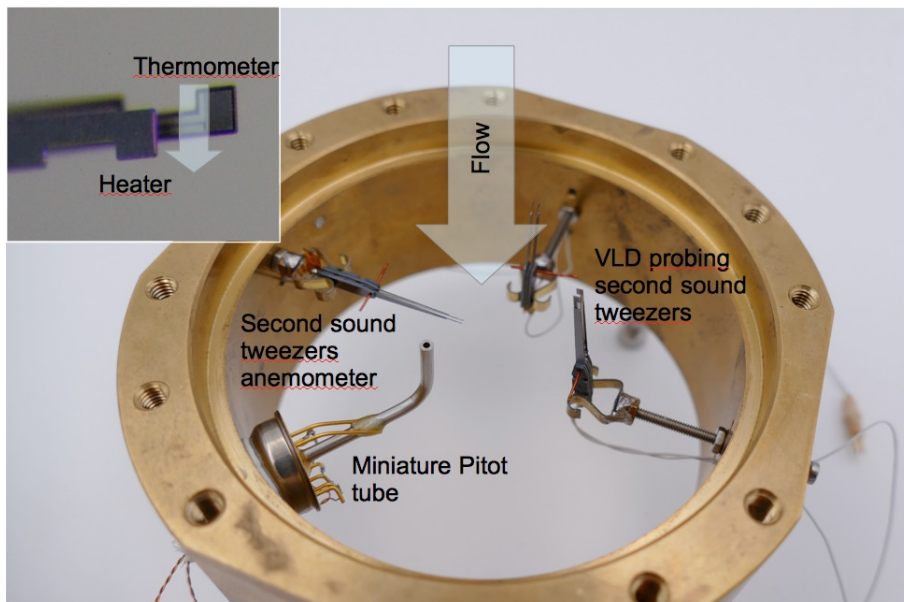


Figure 34: Example of an arrangement of three second sound tweezers dedicated to velocity (x1, left side) and vorticity (x2, right side) time series acquisitions, together with a miniature total head pressure tube (loosely labelled "Pitot tube" on the bottom left side of the picture) used for velocity calibration. All probes are mounted on a ring connecting two 76mm-inner-diameter coaxial pipes (see Fig.1 of ref. [WVR21]). The insert is a close-up of the shifted plates of the anemometer tweezers.

5 Summary and Perspectives

This study has covered three independent topics : the comprehensive analytical modelling of second-sound resonators with a cavity allowing a throughflow of superfluid (section 3), new mathematical methods to process the signal provided by such resonators (section 4) and the miniaturization of immersed second-sound resonators allowing time and/or space resolved flow sensing (section 2). These so-called second-sound tweezers have been used throughout the manuscript to demonstrate the strength and limits of the modelling and analysis methods.

Two observations remains unexplained: the origin of some noise on the acoustic path length and a second order oscillations of the resonator spectral response in quiescent ^4He , named the “daisy effect” (section 3.4.4). Fortunately, both effects don’t impair the measurement of the flow vorticity or velocity.

Some results that were not anticipated when this study was initiated, are worth recalling and discussing:

- the possibility to operate tweezers by over-driving the second-sound standing wave beyond an intrinsic turbulent transition. In this non-linear mode, the probe becomes sensitive to velocity, which is interpreted as a signature of the sweeping of the local vortex tangle by the outer flow (section 2.2.3). This operating mode is somehow analogous of hot film and hot wire anemometry in classical fluid, where sensitivity to velocity is due to the more-or-less pronounced sweeping of the thermal boundary layer around an overheated thermometer.
- in the linear regime (standing wave of small amplitude), the probe can be sized and operated to be either mostly sensitive to quantum vortices or mostly sensitive to the velocity of the throughflow (section 3.5). This prediction is verified experimentally by comparing statistics in turbulent flows (section 4.5). The spatial and time resolution of tweezers operated as anemometers -both in non-linear and linear mode- is close or better than the alternative miniaturized anemometers working in He-II, that is hot-wires [DBM⁺15, DRS⁺21], cantilevers [SMR12, RCSR17b], Pitot tubes [SMR12, RCSR17b] and total head-pressure probes [MT98, WVR21].
- in the absence of throughflow, the full spectral response of the resonators, and in particular its quality factors, can be accurately determined simply taking into account the loss by diffraction and misalignment of the reflecting plates of the cavity. In other words, the other sources of dissipation have negligible contributions in the range of conditions explored here. This is no longer the case in a presence of a throughflow carrying quantum vortices since the latter can significantly contribute to the total dissipation. We have not explored experimentally the production and detection of second-sound by mechanical means, which implies cavity with rough surfaces (e.g. millipore or nucleopore membranes). In this case, the effect of vortices pinned on the surface may no longer be negligible ; for a discussion see [DLL80].
- the possibility to sense the variations of the vortex line density or velocity without knowledge on variations of the second sound velocity (or acoustical path). More generally, the elliptic method allows a mathematical decoupling of both effects by a projection method in the (inverse) complex plane. This results is of major practical interest in flows where the second-sound velocity is not accurately controlled due to residual temperature variations or thermal gradients. This situation can occur for instance in flows sequentially driven at various levels of forcing (e.g. to explore a Reynolds number dependence), in inhomogeneous dissipative flows and in flows close to the lambda superfluid transitions where the second-sound velocities strongly depends of temperature.

Two applications of second-sound tweezers have been illustrated. Measurement within a turbulent boundary layer (Fig. 25) are possible thanks to the small size of probe, and measurements of time series in the bulk of quantum turbulent flow (Fig. 32) are possible thanks to both the time and space resolutions of the probe. Among other applications the probe can map the velocity or the vorticity field of an inhomogeneous flow. A mapping of vorticity in a counterflow jet has been recently done and will be reported elsewhere.

Another application of tweezers would be to probe simultaneously the temperature fluctuations and those of either velocity or vorticity, for instance to explore their correlations in turbulent counterflows or even co-flows. Indeed, the tweezers thermometer provides a direct measurement of temperature in a bandwidth spanning from zero frequency up to a fraction of the frequency of the second sound standing wave, and this signal could be acquired without impairing the measurement of the second sound standing wave. Alternating measurements in the linear and non-linear modes is also interesting to explore locally both velocity and vorticity in a given flow. A last example of application is to operate a double-tweezers made of a heating plate between two thermometer plates, or vice-versa. Such a stack can be used to probe joint statistics of vorticity on one side, and velocity on the other side, or this arrangement can be used alternatively to probe transverse gradient of either vorticity or velocity.

Acknowledgements

We warmly thank our colleague Benoît Chabaud for support during cryogenic tests and operation of the TOUPIE wind-tunnel. We acknowledge and thank the staff of the PTA and Nanofab clean-rooms in Grenoble, where microfabrication was done. Data of figure 25 have been acquired in the SHREK facility. We thank all the members of the SHREK collaboration, in particular Michel Bon Mardion and Bernard Rousset for the specific operation very near the superfluid transition. We acknowledge the indirect but key contribution of A. Elbakyan regarding the comprehensiveness of the bibliography.

The probe design, fabrication, cryogenic operation and theoretical analysis took place over 7 years, and was possible thanks to following research grants: ANR Ecouturb grant (ANR-16-CE30-0016), ANR QUTE-HPC grant (18-CE46-0013- 03) and EU Horizon 2020 Research and Innovation Program "the European Microkelvin Platform (EMP)" (824109).

This research was funded in part by the Agence nationale de la recherche (ANR). A CC-BY public copyright license has been applied by the authors to the present document and will be applied to all subsequent versions up to the Author Accepted Manuscript arising from this submission, in accordance with the grant's open access conditions.

References

- [Bal07] S Balibar. The discovery of superfluidity. *Journal of Low Temperature Physics*, 146(5-6):441–470, 2007.
- [BLR17] J. Bertolaccini, E. Lévêque, and P.-E. Roche. Disproportionate entrance length in superfluid flows and the puzzle of counterflow instabilities. *Phys. Rev. Fluids*, 2:123902, 2017.
- [BSS83] H Borner, T Schmeling, and DW Schmidt. Experimental investigations on fast gold-tin metal film second-sound detectors and their application. *J. Low Temp. Phys.*, 50(5):405–426, 1983.
- [BVS⁺14] S Babuin, E Varga, L Skrbek, E Lévêque, and P-E Roche. Effective viscosity in quantum turbulence: A steady-state approach. *EPL*, 106(2):24006, 2014.
- [CA68] R W. Cohen and B Abeles. Superconductivity in granular aluminum films. *Phys. Rev.*, 168:444–450, 1968.
- [CR83] M J Crooks and B J Robinson. Technique for determining second sound attenuation near the superfluid transition in ^4He . *Review of Scientific Instruments*, 54(1):12–15, 1983.
- [DB98] R J Donnelly and C F Barenghi. The observed properties of liquid helium at the saturated vapor pressure. *Journal of physical and chemical reference data*, 27(6):1217–1274, 1998.
- [DBM⁺15] D. Duri, C. Baudet, J.-P. Moro, P.-E. Roche, and P. Diribarne. Hot-wire anemometry for superfluid turbulent coflows. *Review of Scientific Instruments*, 86(2):025007, 2015.
- [DL77] P E Dimotakis and G A Laguna. Investigations of turbulence in a liquid helium ii counterflow jet. *Physical Review B*, 15:5240, Jun 1977.
- [DLF⁺14] Q. Dong, Y. X. Liang, D. Ferry, A. Cavanna, U. Gennser, L. Couraud, and Y. Jin. Ultra-low noise high electron mobility transistors for high-impedance and low-frequency deep cryogenic readout electronics. *Applied Physics Letters*, 105(1):013504, 2014.
- [DLL80] D D’Humières, A Launay, and Albert Libchaber. Pinning of vortices in nucleopores. effect on second-sound resonators. *Journal of Low Temperature Physics*, 38:207, Jan 1980.
- [Don91] R. J. Donnelly. *Quantized Vortices in Helium-II*. Cambridge Studies in Low Temperature Physics. Cambridge University Press, Cambridge, 1991.
- [Don09] Russell J Donnelly. The two-fluid theory and second sound in liquid helium. *Phys. Today*, 62(10):34–39, 2009.
- [DRS⁺21] P. Diribarne, B. Rousset, Y. A. Sergeev, J. Valentin, and P.-E. Roche. Cooling with a subsonic flow of quantum fluid. *Physical Review B*, 103(14):144509, 2021.
- [FS04] S Fuzier and Steven W Van Sciver. Use of the bare chip cernox(tm) thermometer for the detection of second sound in superfluid helium. *Cryogenics*, 44:211, Mar 2004.

- [Gri09] A Griffin. New light on the intriguing history of superfluidity in liquid⁴He. *Journal of Physics: Condensed Matter*, 21(16):164220, 2009.
- [HL88] K Henjes and M Liu. Peshkov transducers of second sound. *Journal of Low Temperature Physics*, 71(1):97–117, 1988.
- [HR76] J Heiserman and I Rudnick. The acoustic modes of superfluid helium in a waveguide partially packed with superleak. *Journal of Low Temperature Physics*, 22(5):481–499, 1976.
- [HV56a] H. E Hall and W. F Vinen. The rotation of liquid Helium II. i. experiments on the propagation of second sound in uniformly rotating Helium II. *Proceedings of the Royal Society of London. Series A*, 238:204, Dec 1956.
- [HV56b] H. E Hall and W. F Vinen. The rotation of liquid Helium II. II. the theory of mutual friction in uniformly rotating helium II. *Proceedings of the Royal Society of London. Series A*, 238:215, Dec 1956.
- [HVS92] D. S. Holmes and S. W. Van Sciver. Attenuation of second sound in bulk flowing He II. *J. Low Temp. Phys.*, 87:73–93, 1992.
- [HVS01] D.K. Hilton and S.W. Van Sciver. Techniques for the detection of second sound shock pulses and induced quantum turbulence in He II. *Cryogenics*, 41:347–53, 2001.
- [Kem91] R. C. Kemp. The reference function for platinum resistance thermometer interpolation between 13,8033 k and 273,16 k in the international temperature scale of 1990. *Metrologia*, 28(4):327, 1991.
- [Kha00] I M Khalatnikov. *An Introduction to the Theory of Superfluidity*. CRC Press, 2000.
- [Lag76] G. Laguna. Photolithographic fabrication of high frequency second sound detectors. *Cryogenics*, 16(4):241–243, 1976.
- [LFF47] C. T. Lane, Henry A. Fairbank, and William M. Fairbank. Second sound in liquid Helium II. *Phys. Rev.*, 71:600–605, May 1947.
- [Lob07] N Lobontiu. *Dynamics of microelectromechanical systems*. Springer, Boston, MA, 2007.
- [LV74] D Lhuillier and F Vidal. Temperature dependence of the second sound velocity reduction in rotating liquid helium. *Journal of Physics C: Solid State Physics*, 7(14):L254, 1974.
- [Meh74] J. B Mehl. New effects in the interaction of second sound with superfluid vortex lines. *Physical Review A*, 10(2):601, 1974.
- [MG18] B Mastracci and W Guo. An apparatus for generation and quantitative measurement of homogeneous isotropic turbulence in he ii. *Review of Scientific Instruments*, 89(1):015107, 2018.
- [MLM78] RJ Miller, IH Lynall, and JB Mehl. Velocity of second sound and mutual friction in rotating helium ii. *Physical Review B*, 17(3):1035, 1978.
- [MMP⁺07] V. F Mitin, PC McDonald, F Pavese, NS Boltovets, VV Kholevchuk, IY Nemish, VV Basanets, VK Dugaev, PV Sorokin, and RV Konakova. Ge-on-gaas film resistance thermometers for cryogenic applications. *Cryogenics*, 47(9-10):474–482, 2007.
- [MPS84] P Mathieu, B Plaçais, and Y Simon. Spatial distribution of vortices and anisotropy of mutual friction in rotating He II. *Physical Review B*, 29:2489, Mar 1984.
- [MSS76] P. Mathieu, A. Serra, and Y. Simon. Critical-region measurements of the mutual-friction parameters in rotating He II. *Phys. Rev. B*, 14:3753–3761, 1976.
- [MT98] J. Maurer and P. Tabeling. Local investigation of superfluid turbulence. *Europhys. Lett.*, 43(1):29–34, 1998.
- [NF95] S. K. Nemirovskii and W. Fiszdon. Chaotic quantized vortices and hydrodynamic processes in superfluid helium. *Rev. Modern Phys.*, 67:37–84, 1995.
- [Not64] H A Notarys. *Megacycle frequency second sound*. PhD thesis, California Institute of Technology, 1964.
- [Pes46] V. P. Peshkov. Determination of the velocity of propagation of the second sound in helium ii. *Journal of Physics (Moscow)*, 10:389, 1946.

- [Pes48] VP Peshkov. Propagation of second sound in helium ii. exp. *Zh. Eksp. Teor. Fiz.*, 18:857, 1948.
- [PGB70] R. L St Peters, T. J. Greytak, and G.B. Benedek. Brillouin scattering measurements of the velocity and attenuation of high frequency sound waves in superfluid helium. *Optics Communications*, 1(9):412–416, 1970.
- [PK82] DB Poker and CE Klabunde. Temperature dependence of electrical resistivity of vanadium, platinum, and copper. *Physical Review B*, 26(12):7012, 1982.
- [Put74] S J Putterman. Superfluid hydrodynamics. *Series in low temperature physics*, 3, 1974.
- [RBD⁺14] B. Rousset, P. Bonnay, P. Diribarne, A. Girard, J.M. Poncet, E. Herbert, J. Salort, C Baudet, B Castaing, L. Chevillard, F. Daviaud, B. Dubrulle, Y. Gagne, M. Gibert, B. Hébral, T. Lehner, P.-E. Roche, B. Saint-Michel, and M Bon Mardion. Superfluid high Reynolds von Kármán experiment. *Rev. Sci. Instrum.*, 85:103908, 2014.
- [RCSR17a] E Rusaouen, B Chabaud, J Salort, and P-E Roche. Intermittency of quantum turbulence with superfluid fractions from 0% to 96%. *Phys. Fluids*, 29(10):105108, 2017.
- [RCSR17b] E. Rusaouen, B. Chabaud, J. Salort, and P.-E. Roche. Intermittency of quantum turbulence with superfluid fractions from 0% to 96%. *Phys. Fluids*, 29(10):105108, 2017.
- [RDD⁺07] P-E Roche, Pantxo Diribarne, Thomas Didelot, Olivier Français, Lionel Rousseau, and Hervé Willaime. Vortex density spectrum of quantum turbulence. *EPL (Europhysics Letters)*, 77(6):66002, 2007.
- [RG84] M. Raui and A. Guenter. Damping of second sound near the superfluid transition of 4He as a function of pressure. *Physical Review B*, 30:5116, Nov 1984.
- [RR01] D Rinberg and M L Rappaport. Fiber bolometer and emitter with negligible reflection for second sound measurements near the lambda-point. *Cryogenics*, 41(8):557–561, 2001.
- [Sad98] J E Sader. Frequency response of cantilever beams immersed in viscous fluids with applications to the atomic force microscope. *Journal of Applied Physics*, 84(1):64–76, 1998.
- [SCLR12] J. Salort, B. Chabaud, E. Lévêque, and P.-E. Roche. Energy cascade and the four-fifths law in superfluid turbulence. *EPL*, 97:34006, 2012.
- [SE70] R. A Sherlock and D. O Edwards. Oscillating superleak second sound transducers. *Rev. Sci. Instrum.*, 41:1603, Jan 1970.
- [SHVS99] M.R. Smith, D.K. Hilton, and S. W. Van Sciver. Observed drag crisis on a sphere in flowing He I and He II. *Phys. Fluids*, 11:751–3, 1999.
- [SMR12] J. Salort, A. Monfardini, and P.-E. Roche. Cantilever anemometer based on a superconducting micro-resonator: Application to superfluid turbulence. *Rev. Sci. Instrum.*, 83:125002, 2012.
- [SNVD02] S.R. Stalp, J. J Niemela, W. J. Vinen, and R. J. Donnelly. Dissipation of grid turbulence in helium II. *Phys. Fluids*, 14:1377–9, 2002.
- [Sny62] H. A. Snyder. Use of germanium as a second sound receiver. *Review of Scientific Instruments*, 33(4):467–469, 1962.
- [SP66] H. A. Snyder and Zimri Putney. Angular dependence of mutual friction in rotating Helium II. *Phys. Rev.*, 150:110, 1966.
- [SPB17] GW Stagg, NG Parker, and CF Barenghi. Superfluid boundary layer. *Physical Review Letters*, 118(13):135301, 2017.
- [Tou82] J. T. Tough. *Superfluid Turbulence*, volume 8, chapter 3, pages 133–219. North-Holland Publishing Company, Amsterdam, 1982.
- [Tsa62] D.S. Tsakadze. (sov. phys. jetp 15 (1962) 681). *Zh. Eksp. Teor. Fiz.*, 42:985, 1962.
- [VBL⁺17] E Varga, S Babuin, VS L’vov, Anna Pomyalov, and L Skrbek. Transition to quantum turbulence and streamwise inhomogeneity of vortex tangle in thermal counterflow. *Journal of Low Temperature Physics*, 187(5-6):531–537, 2017.

- [Vin57] W. F Vinen. Mutual friction in a heat current in liquid helium ii. iii. theory of the mutual friction. *Proceedings of the Royal Society of London. Series A*, 242:493, Nov 1957.
- [VJSS19] E Varga, MJ Jackson, D Schmoranzler, and L Skrbek. The use of second sound in investigations of quantum turbulence in He II. *J. Low Temp. Phys.*, 197(3):130–148, 2019.
- [VS71] F Vidal and Y Simon. Ideal second sound resonance in he-ii. *Physics Letters A*, 36(3):165–166, 1971.
- [WBF⁺69] R. Williams, S.E.A. Beaver, J.C. Fraser, R.S. Kagiwada, and I. Rudnick. The velocity of second sound near λ . *Physics Letters A*, 29(5):279–280, 1969.
- [WPHE81] P. E. Wolf, B. Perrin, J. P. Hulin, and P. Elleaume. Rotating Couette flow of helium II. *J. Low Temp. Phys.*, 44:569–593, September 1981.
- [WVR21] E Woillez, J Valentin, and P-E Roche. Local measurement of vortex statistics in quantum turbulence. *EPL (Europhysics Letters)*, 134(7):46002, 2021.
- [YI18] J Yang and GG Ihas. Decay of grid turbulence in superfluid helium-4: Mesh dependence. In *Journal of Physics: Conference Series*, volume 969, page 012004. IOP Publishing, 2018.
- [YIE17] J. Yang, G. G Ihas, and D. Ekdahl. Second sound tracking system. *Review of Scientific Instruments*, 88(10):104705, 2017.
- [YYK97] T Yotsuya, M Yoshitake, and T Kodama. Low-temperature thermometer using sputtered zrx thin film. *Cryogenics*, 37(12):817–822, 1997.